LBL-19769

RECEIVED BY OSTI OCT 09 1985

Lawrence Berkeley Laboratory
UNIVERSITY OF CALIFORNIA

Materials & Molecular
Research Division

# ELECTRON ENERGY LOSS SPECTROSCOPY OF $CH_3N_2CH_3$ ADSORBED ON Ni(100), Ni(111), Cr(100), Cr(111)

M.A. Schulz
(M.S. Thesis)

July 1985

Prepared for the U.S. Department of Energy under Contract DE-AC03-76SF00098

LBL--19769

DE86 000605

# ELECTRON ENERGY LOSS SPECTROSCOPY OF $CH_3N_2CH_3$ ADSORBED ON Ni(100), Ni(111), Cr(100), Cr(1 1)

Margaret A. Schulz
(M.S. Thesis)

Materials and Molecular Research Division
Lawrence Berkeley Laboratory

and

Department of Chemistry
University of California
Berkeley, California 94720

July 1985



This work was supported by the Director, Office of Energy Research, Office of Basic Energy Sciences, Chemical Sciences Division of the U.S. Department of Energy under Contract No. DE-AC03-76SF00098.

# I. INTRODUCTION

Chapter II presents a study of the adsorption of $CH_3N_2CH_3$ on Ni(100), Ni(111), Cr(100), and Cr(111) using high resolution electron energy loss spectroscopy (EELS). Under approximately the same conditions of coverage, the vibrational spectra of $CH_3N_2CH_3$ on these four surface are quite distinct from one another, implying that the $CH_3N_2CH_3$-substrate interaction is very sensitive to the physical and electronic structure of each surface. In addition to the room temperature studies, the evolution of surface species on the Ni(100) surface in the temperature range 300 to 425 K was studied. Analysis of the Ni(100) spectra indicates that molecular adsorption, probably through the N lone pair, occurs at room temperature. Spectra taken after annealing the $CH_3N_2CH_3$-Ni(100) surfaces indicate that CH and CN bond scission occurred at the elevated temperatures. Decomposition of $CH_3N_2CH_3$ takes place on the Ni(111), Cr(100), and Cr(111) surfaces at room temperature, as evidenced by the intensity of the carbon-metal stretch in the corresponding spectra. Possible identities of coadsorbed dissociation products are considered. The stable coverage of surface species on all four surfaces at 300 K is less than one monolayer.

Chapter III begins with a general description of an electron energy loss (EEL) spectrometer followed by a more specific discussion of some recent modifications to the EEL monochromator assembly used in this laboratory. Both the previous configuration of our monochromator and the new version are briefly described, as an aid to understanding

the motivation for the changes as well as the differences in operation of the two versions. For clarity, the new monochromator design is referred to as variable pass, while the previous design is referred to as double pass. A modified tuning procedure for the new monochromator is also presented.

## II. ADSORPTION of $CH_3N_2CH_3$ on Ni(100), Ni(111), Cr(100), and Cr(111).*

### A. Introduction

High resolution electron energy loss spectroscopy (EELS) is a powerful tool in the vibrational analysis of atoms and molecules adsorbed on solid surfaces.[1] The vibrational spectra obtained in EELS provide chemical and geometrical information about adsorbed species. The technique has proven especially useful in the study of hydrocarbon adsorption on well characterized metal surfaces. A variety of unsaturated hydrocarbon-transition metal systems has been studied, mainly because of the catalytic importance of such systems. Ethylene, acetylene, and benzene, for example, are among the most frequently studied hydrocarbon adsorbates.[2-11] Molecules such as these, containing unsaturated carbon-carbon bonds, can interact strongly with the metal surface through their $\pi$-electron systems. This type of interaction with the metal surface can lead to rehybridization or fragmentation of the adsorbate.[12,13] The adsorption and subsequent reaction of unsaturated hydrocarbon molecules on well characterized transition metal surfaces can be studied using electron energy loss spectroscopy to identify adsorbed species or reactive intermediates.

In addition to the adsorption of unsaturated hydrocarbons, the adsorption on transition metal surfaces of molecules containing lone electron pairs has generated a great deal of interest. Molecules such as CO, $NH_3$, $CH_3OH$, and $CH_3NH_2$ can bond to a metal surface by

donation of a lone electron pair.[14-18] This type of adsorption tends to be weaker than that experienced by unsaturated hydrocarbons, and in many of these systems the adsorbate is only weakly perturbed from its gas-phase geometry and hybridization. Desorption of the adsorbate competes with reaction or decomposition on the surface.

More recently, the adsorption of molecules with both aromatic and lone pair electrons has been studied. Pyridine and thiophene are two adsorbates of this type.[19,20] In these systems, bonding can occur through both the lone pair and through the π-electron system, depending on conditions of surface coverage and temperature.[21,22]

No previous studies have been reported on the adsorption of trans-1,2-dimethyldiazene (t-$CH_3N_2CH_3$), or azomethane, on clean, well characterized, transition metal surfaces. Azomethane is of interest as an adsorbate because it has the potential of interacting with a metal surface in both of the ways discussed above. Coordination to the surface may occur through donation of either of the two lone electron pairs. Or, a stronger adsorbate-surface interaction may occur involving rehybridization of the azo (N=N) linkage and, possibly, rearrangement or fragmentation of the azomethane. The latter type of interaction would be particularly interesting as it has not yet been observed for a N=N system adsorbed on a transition metal surface. Examples of both types of interaction have been observed in organometallic complexes containing ligands which are coordinated to the metal center through an azo linkage.[23-28] The most closely related adsorption system which has

been studied was $CH_2N_2$ on Ru(001) by George et al., but in that work no conclusions were drawn about the N≡N interaction with the surface.[29] Comparisons between the adsorption of $CH_3N_2CH_3$ and the adsorption of molecules containing a >C=C< or a >C=N- function, or of molecules such as $CH_3NC$, $CH_3CN$, $N_2$, and $CH_3NH_2$ would also be of interest.[18,30-33]

Cr and Ni surfaces were chosen for the adsorption study of $CH_3N_2CH_3$ because of their very different reactivities with respect to other adsorbates. CO, for example, completely dissociates on the structurally different low index surfaces of Cr at all coverages at 300 K.[34,35] On Ni, however, CO does not dissociate on either the low index surfaces[36] or on steps[37] at any temperature up to the desorption temperature of CO (450 K). Structurally dissimiliar surfaces of each metal were studied to isolate effects due to structural rather than electronic properties. Since nickel has an fcc structure while chromium has a bcc structure, corresponding faces of the two crystals do not have the same geometrical structure. The nickel surfaces are flat with only one layer of metal atoms exposed; the Ni(111) surface is more densely packed than the Ni(100) surface. The chromium surfaces are relatively open. On Cr(100) both first and second layer metal atoms are exposed, while on Cr(111), first, second, and third layer atoms are exposed.

The experimental procedures are discussed in section B. The results of a vibrational study of $CH_3N_2CH_3$ adsorbed on the Ni(100), Ni(111), Cr(100), and Cr(111) surfaces are discussed in

separate subsections of section C. In sections C-1 and C-2, the energy loss spectra of azomethane adsorbed on Ni(100) indicate that the majority species present on the surface at 300 K is molecular azomethane, although some of the vibrational frequencies of chemisorbed $CH_3N_2CH_3$ may be strongly shifted from those of the free molecule. Brief anneals of the $CH_3N_2CH_3$-Ni(100) surfaces result in decomposition of the azomethane (section C-3). The spectra of $CH_3N_2CH_3$ on Ni(111) (section C-4) and Cr(100) (section C-5) indicate that appreciable decomposition of the $CH_3N_2CH_3$ occurs on these surfaces at 300 K. The complexity of the spectra, coupled with the possibility of strong frequency shifts in the vibrational modes of the molecular species, creates ambiguities in the assignment of several peaks, however. Correlations with the gas-phase spectrum of azomethane and with the surface spectra of related molecules are made. The spectrum of $CH_3N_2CH_3$ adsorbed on the Cr(111) surface (section C-5) exhibits a relatively small number of loss peaks and indicates that complete decomposition of the azomethane has occurred. The conclusions are summarized in section D.

## B. Experimental

Energy loss spectra were obtained using a double pass monochromator and a single pass analyzer which typically provide an energy resolution of 50-70 $cm^{-1}$ FWHM. The EEL spectrometer is briefly described in the next chapter of this paper. A detailed description can be found in reference 38. The spectrometer is housed

in a stainless steel vacuum chamber which is also equipped for Auger electron spectroscopy (AES), low energy electron diffraction (LEED), quadrupole mass spectroscopy, and ion sputtering. The incident beam energy was chosen to optimize the signal and for these studies ranged from 2.0 to 2.5 eV. Both specular and off-specular measurements were made. The scattering geometry will be indicated separately for each measurement (section C).

The single crystals were cut and polished by standard methods. Both the Ni and Cr crystals were precleaned using argon ion sputtering with repetitive cycling of the crystal temperature (between 300 and 1075 K for the Ni crystals and between 300 and 1175 K for the Cr crystals). Between adsorption experiments, the crystals were sputtered, then exposed to 2 L of oxygen and flashed to a high temperature (1075 K for Ni, 1175 K for Cr). The Cr surfaces required another sputter/anneal cycle to remove the oxygen. Surface cleanliness and ordering were monitored using Auger spectroscopy (with a retarding field analyzer) and LEED, respectively. The crystal temperature was monitored with a chromel-alumel thermocouple spot-welded to the sample plate or with an optical pyrometer.

Trans-1,2-dimethyldiazene was prepared by the oxidation of 1,2-dimethylhydrazine ($CH_3NHNHCH_3$) using mercuric oxide. The 1,2-dimethylhydrazine was obtained by treating the dihydrochloride salt (Aldrich) with sodium hydroxide and water.[39] The end product, $CH_3N_2CH_3$ (mp = -78 C, bp = 1.5 C), was purified by several freeze-pump-thaw cycles and introduced into the ultra high vacuum

chamber (base pressure 2 X $10^{-10}$ torr) by means of an effusive beam doser which could be directed at the sample. Its purity was checked before introduction into the chamber by infrared spectroscopy and in situ by mass spectrometry. $CH_3Cl$ and, occasionally, small amounts of CO were detected in the IR spectra. Careful purification resulted in elimination of the CO (no increase in the mass 28 peak was observed when the azomethane was admitted to the chamber), but the mass spectra indicated that a small quantity of $CH_3Cl$ was usually admitted into the chamber with the $CH_3N_2CH_3$. Electron energy loss spectra of pure $CH_3Cl$ were taken at several coverages and temperatures on all four surfaces studied, but, other than a weak C-metal stretch, no vibrational features were observed.

Gas-phase $CH_3N_2CH_3$ belongs to the $C_{2h}$ symmetry point group. The twelve normal modes belonging to the $a_g$ and $b_g$ representations are Raman active; the twelve belonging to the $a_u$ and $b_u$ representations are IR active. Twenty-two of the twenty-four normal modes have been unambiguously assigned using IR and Raman data for gas- and solid-phase $CH_3N_2CH_3$.[40-42] There is some uncertainty in the literature regarding the assignment of $\nu_{22}$, the asymmetric CN stretch, and $\nu_{23}$, a $CH_3$ rock. Durig et al. assigned the CN stretch to a very weak feature at 1300 (1330) $cm^{-1}$ in the gas- (solid-)phase IR spectrum (none of the other workers reported this feature), and they assigned the $CH_3$ rock to a peak at 1001 $cm^{-1}$.[40] Pearce et al. assigned the 1001 $cm^{-1}$ peak to the CN stretch and concluded that the $CH_3$ rock was unobserved.[41] Craig

et al. assigned the 1001 $cm^{-1}$ peak to the $CH_3$ rock and predicted that the CN stretch is degenerate with $\nu_{15}$, a methyl rock occurring at 1111 $cm^{-1}$.[42] They calculated a frequency of 1112 $cm^{-1}$ for the CN stretch.

C. Results and Discussion

The spectra of azomethane on Ni(100) will be discussed in detail before the spectra of azomethane adsorbed on the Ni(111), Cr(100), and Cr(111) surfaces are presented. Associative adsorption is believed to be the primary adsorption process on Ni(100) at room temperature. Both specular and off-specular measurements of the $CH_3N_2CH_3$-Ni(100) system support this model. Spectra of several annealed $CH_3N_2CH_3$-Ni(100) surfaces illustrate that measureable decomposition of the $CH_3N_2CH_3$ occurs on Ni(100) at elevated temperatures. Irreversible C-H bond cleavage is postulated as the initial step in the thermal decomposition process.

The spectra of azomethane on Ni(111), Cr(100), and Cr(111) indicate that dissociative adsorption occurs on these surfaces at 300 K. A mixture of coadsorbed decomposition products is proposed for the Ni(111) and Cr(100) surfaces, although the presence of some molecular azomethane cannot be ruled out. The simplicity of the $CH_3N_2CH_3$-Cr(111) spectrum implies that, aside from atomic adsorbates, only a single chemisorbed species is present on this surface.

1. $CH_3N_2CH_3$-Ni(100), Specular and Off-specular Data.

There are two major scattering mechanisms in electron energy loss spectroscopy, dipole scattering and impact scattering.[43,44] The dipole selection rule states that only those vibrational modes belonging to the totally symmetric representation of the point group of the adsorbate complex are active in the specular direction. Dipole scattering is strongly peaked in the specular direction, and the intensity of loss features is proportional to the elastically scattered intensity. Modes excited by the short-range impact mechanism are not restricted to those belonging to the symmetric representation of the adsorbed species. Such modes exhibit a much broader and flatter angular distribution than do dipole modes, but their intensity in the specular direction is usually much less than that of losses due to dipole scattering. Hence, modes which are principally excited by the long-range dipole mechanism are expected to dominate spectra taken in the specular direction. The intensity of impact losses is proportional to the incident electron current but, unlike the dipole scattering intensity, not to the elastically scattered intensity. Anything which lowers the observed elastic intensity, such as collection at angles other than the specular or a decrease in surface order, will lower the intensity of dipole-allowed inelastic features but will not necessarily change the intensity of the impact scattering features, provided that the incident electron current remains the same. A relative increase in the intensity of the impact excited modes is then observed.

Figure 1 shows the vibrational loss spectra for a saturation coverage of $CH_3N_2CH_3$ on Ni(100) taken in the specular direction and 15° away from the specular direction at room temperature. Azomethane exposed to this surface reaches a saturation coverage after which no major changes in the spectra, other than a gradual decrease in the total signal, are observed with further exposure. Absolute exposures could not be determined, but coverages of azomethane on all four surfaces are believed to be less than one monolayer based on the strong Ni/Cr signals relative to the C and N signals in the Auger spectra and comparison of the relative intensities to those of systems with known N and C coverages.

The most striking differences between the specular and off-specular spectra in Figure 1 are (1) the greater (~4X) intensity of eight of the losses in the off-specular spectrum, (2) the appearance of a broad, asymmetric band between 2790 and 3000 $cm^{-1}$ in this spectrum, and (3) the changes in the relative intensities of the other peaks in the spectra, notably the peaks occurring at 1066 and 1408 $cm^{-1}$. These differences indicate that the higher frequency modes are principally excited by the impact mechanism and that all the modes, except that responsible for the 530 $cm^{-1}$ loss, have strong impact contributions.

Enhancement of the impact scattering contribution to the observed vibrational modes is also illustrated in Figure 2, which compares spectra of a Ni(100) surface after two exposures differing by a factor of 10 in the amount of azomethane admitted into the chamber. Both

spectra were taken in the specular direction. The greater exposure has two effects: It causes a marginal increase in the surface coverage, as indicated by a comparison of the relative Auger spectral intensities for the surfaces, and it induces disorder, as evidenced by a two-fold decrease in the count rate of the elastic peak in the high-exposure spectrum. The surface disorder favors impact scattering relative to dipole scattering, as can be seen by the similarity between the off-specular spectrum in Fig. 1 and the high-exposure spectrum in Fig. 2.

Assignments of the $CH_3N_2CH_3$-Ni(100) spectra are summarized in Table 2. These assignments will be discussed in detail in section C-2. Seven of the nine peaks in the Ni(100) spectra can be attributed to molecular azomethane. The broad, asymmetric band between 2790 and 3000 $cm^{-1}$ in the off-specular $CH_3N_2CH_3$-Ni(100) spectrum results from symmetric and asymmetric C-H stretches and will be discussed later in this section.

The $C_{2h}$ symmetry of the gas-phase $CH_3N_2CH_3$ is lowered to either $C_1$ or $C_s$ symmetry upon adsorption at the Ni(100) surface, because the center of inversion and the $C_2$ axis are lost. The symmetry plane containing the C-N=N-C skeleton and bisecting the two $CH_3$ groups may ($C_s$) or may not ($C_1$) exist as such in the adsorbed species, depending on its orientation, the site geometry, and the strength of the adsorbate-surface interaction. In the case of $C_s$ symmetry, 18 "internal" modes would be dipole active, while for $C_1$ symmetry, 24 "internal" modes would be dipole active. Thus, for

spectra collected in the specular direction, these dipole-allowed modes should be the most intense. For a number of reasons, however, it is unlikely that EELS, at its present level of resolution, can be used to determine the symmetry of $CH_3N_2CH_3$ adsorbed on any of the surfaces studied. These reasons are discussed below.

For any adsorbate containing a large number of atoms, it is unlikely that all the dipole-allowed modes can be observed. The instrumental broadening, as well as line broadening due to adsorbate-surface or adsorbate-adsorbate interactions, limits the effective resolution of the spectrometer. Hence, modes which are close in frequency may not be separately resolved in the EEL spectrum. Furthermore, the intensity of a given mode depends on the magnitude of its dynamic dipole as well as on its symmetry. Modes with a weak dynamic dipole can be difficult or impossible to observe in the specular direction. The number of active modes may depend on the adsorption site, especially if the adsorbate-substrate interaction is strong. The complexity of the vibrational spectrum will increase if the adsorbate bonds to the surface at a variety of sites or if several different species are present on the surface. Finally, the possibility that an impact mode is coincident in frequency with a dipole mode, and hence "not observed" in the off-specular direction, must be considered. For these reasons, it may not be possible to determine the symmetry of an adsorbed species, especially one containing a large number of atoms such as $CH_3N_2CH_3$, from a specular EEL spectrum.

A comparison of specular and off-specular spectra can be more fruitful, especially if only the two symmetry species $C_1$ and $C_s$ are possible. The appearance of a mode only in the off-specular direction would imply that this mode, primarily excited via an impact scattering mechanism, is probably not associated with the totally symmetric representation. Therefore, the adsorbate complex would have $C_s$ symmetry. Unfortunately, this argument does not hold for $CH_x$ ($x = 1,2,3$) stretching modes, which often have small dynamic dipoles. In other words, the fact that these modes are often weak or absent in the specular direction as in the $CH_3N_2CH_3$-Ni(100) spectra may not be a selection-rule effect. In any case, $C_s$ symmetry is sufficiently low to allow a perpendicular component of a dipole moment connected with a $CH_x$ stretching vibration. Thus, a comparison of the $CH_3N_2CH_3$-Ni(100) specular and off-specular spectra does not allow determination of the symmetry of the adsorbate complex. It does, however, confirm the existence of $CH_x$ species, and it provides some information about their environment.

2. Assignment of $CH_3N_2CH_3$-Ni(100) Spectra.

The simplest adsorption model invokes molecular adsorption of the $CH_3N_2CH_3$ through one of the N lone pairs with relatively little perturbation of the azomethane from its gas-phase geometry. This is not an unreasonable first assumption. A number of organometallic complexes containing ligands with azo functional groups are known.[45-48] In some of these complexes, the azo linkage is

coordinated to one or two metal centers through one or both N lone pairs, with little change in the ligand geometry from its gas-phase geometry.[49] The bond lengths and bond angles of molecular azomethane are such that molecular adsorption on Ni(100) could occur, although some of the hydrogens would be in close proximity to the surface.[42]

The most straightforward way to determine the feasibility of this initial model is to compare the surface spectra with the gas-phase spectra of azomethane. When this comparison is made, two questions should be kept in mind: How do the observed vibrational modes of the surface complex relate to the vibrational modes of the gas-phase molecule? And, are there (or should there be) any additional modes in the spectrum of the adsorbate complex? Another comparison which may be useful is that between the surface spectra of adsorbed azomethane and the infrared spectra of organometallic complexes which contain azomethane or related molecules as ligands.

In many cases, the agreement between surface spectra and gas-phase spectra of a given molecule is quite good, which certainly facilitates identification of the adsorbed species. Of course, even if the $CH_3N_2CH_3$ adsorbs molecularly, there can be differences between the gas-phase and surface spectra. A general rule of thumb maintains that the stronger the interaction between the substrate and the adsorbate, the weaker will be the correspondance between the surface and gas-phase spectra. If the interaction is sufficiently strong, it will affect the "internal" geometry and bonding of the

adsorbate complex, and these changes will, at the very least, be reflected as frequency shifts or intensity differences in the vibrational spectrum of the adsorbate. If the interaction is so strong that a surface reaction occurs, the vibrational spectrum of the surface complex and that of the gas-phase molecule may not correspond at all. The strength of the adsorbate-substrate interaction is not the only factor which determines the energy loss spectrum. The relative contributions of impact and dipole scattering to each mode, as well as the magnitude of the dynamic dipole for each mode and the overall symmetry of the adsorbate complex, are also contributing factors to the observed spectrum.

The second question is somewhat easier to answer. A non-linear polyatomic molecule has (3N - 6) normal modes in the gas-phase. If that molecule adsorbs molecularly onto a metal surface, which in the simplest case is considered as a hard wall, 3N normal modes are possible. The translations and rotations of the adsorbed molecule experience a restoring force, so they have a nonzero frequency. These "new" modes are often referred to as "frustrated" translations or "frustrated" rotations, and they tend to occur at low frequencies. Again, the number of modes observed in an EEL spectrum depends on the symmetry of the adsorbate complex, the strength of the adsorbate-substrate interaction, the magnitude of the dynamic dipole for each transition, and the frequency at which the modes occur. Low frequency modes tend to be obscured by the tailing of the elastic peak. Furthermore, if two modes are close in frequency, within 50

$cm^{-1}$, they will probably not be resolved as two features in the EEL spectrum.

The $CH_3N_2CH_3$-Ni(100) spectra were assigned primarily by comparison with the IR and Raman spectra of gas- (and solid-)phase azomethane.[40-42] The IR and Raman data are summarized in Table 1 and the surface spectra in Table 2. Seven of the nine peaks correspond to vibrational modes of molecular $CH_3N_2CH_3$. One peak, at 795 $cm^{-1}$ cannot be definitively assigned. The ninth peak, at 328 $cm^{-1}$ is assigned to the carbon-metal stretch. The linewidths in the energy loss spectra are all broad; some of the peaks could result from overlapping vibrational modes.

In gas-phase azomethane, there are six methyl stretching vibrations, four asymmetric ($\nu_1$, $\nu_9$, $\nu_{13}$, and $\nu_{18}$) and two symmetric ($\nu_2$ and $\nu_{19}$). All occur at different frequencies in the narrow range between 2911 $cm^{-1}$ and 2989 $cm^{-1}$ $cm^{-1}$, although the asymmetric modes occur at slightly higher frequencies than do the symmetric modes, ~2975 vs ~2920 $cm^{-1}$. Even if the azomethane adsorbed on the surface in such a way that all six modes were dipole active and occured at frequencies that were relatively unperturbed from their gas-phase values, it is unlikely that one could do more than distinguish the symmetric from the asymmetric modes using an EEL spectrometer. Similarly, of the six methyl deformations, it is unlikely that one could do more than separate the asymmetric ($\nu_4$, $\nu_{10}$, $\nu_{14}$, and $\nu_{20}$) from the symmetric modes ($\nu_5$, $\nu_{21}$), if that. As with the methyl stretches, the asymmetric methyl

deformations generally occur at somewhat higher frequencies than the symmetric modes, ~1435 vs ~1385 $cm^{-1}$.

There are four methyl rocking modes in gas-phase azomethane. Three have been unambiguously observed in the IR and Raman spectra ($\nu_7$, $\nu_{11}$, and $\nu_{15}$ at 916, 1026, and 1112 $cm^{-1}$ respectively). If these modes occured with sufficient intensity and if no interfering peaks were present in the same spectral region, they could be distinguished in an EELS spectrum. The fourth (unidentified) methyl rock ($\nu_{23}$) probably occurs in the 1000-1200 $cm^{-1}$ region of the spectrum.

Six fundamentals of gas-phase azomethane result primarily from heavy atom motions and include a N=N stretch ($\nu_3$), symmetric ($\nu_6$) and asymmetric ($\nu_{22}$) CN stretches, and one symmetric ($\nu_8$) and two asymmetric ($\nu_{16}$, $\nu_{24}$) CNN bending modes. The CNN bends all occur at low frequencies; the symmetric mode at 584 $cm^{-1}$, and the two asymmetric modes at 312 and 362 $cm^{-1}$. The N=N stretch occurs at about 1580 $cm^{-1}$ in the Raman spectrum. Finally, the asymmetric CN stretch, which has not been definitively assigned in the gas-phase spectrum, is calculated to fall in about the same region of the spectrum as the unidentified $CH_3$ rocking mode. The symmetric CN stretch, at 1180 $cm^{-1}$, also falls in a region of the spectrum containing peaks from $CH_3$ rocking motions ($\nu_{15}$ and possibly $\nu_{23}$). The two lowest frequency modes have been observed only in the solid-phase IR and Raman spectra. They correspond to the methyl group torsions, $\nu_{12}$ and $\nu_{17}$. These fundamentals occur in a region of

the spectrum which is inacessible to most EEL spectrometers (i.e., below 300 $cm^{-1}$).

In the simple adsorption model discussed above, the azomethane adsorbs molecularly through a N lone pair. An additional six modes, not found in the gas-phase spectrum, are possible, although they may not all be dipole-allowed. These modes are the frustrated translations and rotations of the azomethane on the Ni(100) surface and are expected to occur at low frequencies. For most adsorbed species, usually only the frustrated translation in the z direction (i.e., the metal-adsorbate stretch) and perhaps one or two frustrated rotations occur with sufficient intensity to be observed.

If molecular adsorption occurs on the Ni(100) surface at 300 K, the shoulder at 530 $cm^{-1}$ may correspond to the CNN bend, although this frequency is shifted 50 $cm^{-1}$ down from the gas-phase frequency. Downshifts of similar magnitude were observed in the frequency of the CNN bend of $CH_2N_2$ adsorbed on Ru(001).[29] The other plausible assignment for this loss would be a N-Ni stretch, although this loss has not been unambiguously assigned for any adsorbate on Ni(100). The lack of a definite N-metal stretch cannot be taken as evidence that the $CH_3N_2CH_3$ is <u>not</u> bonded to the surface through a N lone pair. This mode has not been positively observed in other systems, $CH_3NH_2$-Ni(100)[18], $NH_3$-Ni(111)[15], or $CH_3CN$-Ni(111)[31] for example, in which the adsorbate is believed to bond to the metal through the N lone pair.

The low intensity peak at 795 $cm^{-1}$ could correspond to a methyl

rock ($\nu_7$, $\nu_{11}$, or $\nu_{23}$), although, if this is the case, the frequency has shifted at least 120 $cm^{-1}$ down from its gas-phase value. Avery et al. observed a methyl rock at 990 $cm^{-1}$ for acetone adsorbed on Ru(001) in a side-on configuration and (another) at 910 $cm^{-1}$ for acetone on Pt(111), bonded to the surface through the oxygen atom.[50] The corresponding gas-phase frequencies for acetone are 1066 and 902 $cm^{-1}$, respectively. Sexton et al. partially attributed a band at 1040 $cm^{-1}$ in the spectrum of $(CH_3)_2SO$ adsorbed on Pt(111) to a methyl rock.[51] The corresponding gas-phase frequency is 930-950 $cm^{-1}$. Hence, frequency shifts of 70-100 $cm^{-1}$ for these modes are not uncommon.

The peak at 795 $cm^{-1}$ could also be attributed to a fragment species. Demuth et al. identified a CH surface species on Ni(111), which was stable between room temperature and 450 K.[12] This species exhibited a CH bending mode at 790 $cm^{-1}$ and could be responsible for the 795 $cm^{-1}$ peak observed in the $CH_3N_2CH_3$-Ni(100) spectra. If a CH species is present on the surface, a CH stretching frequency higher than 2960 $cm^{-1}$ would also be expected. The change in the hybridization of the C atom from $sp^3$ to $sp^2$ or sp would result in an upward frequency shift of the CH stretching modes. (The CH stretching frequency reflects the degree of hybridization of the C atom. For $sp^3$ hybridized carbon, the CH stretch should occur between 2775 and 2985 $cm^{-1}$. The CH stretch of an $sp^2$ hybridized carbon occurs between 2960 and 3250 $cm^{-1}$, while that for an sp hybridized carbon occurs around 3250 to 3350 $cm^{-1}$.) Demuth et

al.[12] observed a CH stretch at 2980 $cm^{-1}$, which is slightly greater than the frequency one would expect for an $sp^3$ hybridized carbon. Furthermore, they claimed that the frequency of the bend observed for the CH species on Ni(111), 790 $cm^{-1}$, is characteristic of a hybridization of the carbon between sp and $sp^2$. The CH stretching region in the off-specular $CH_3N_2CH_3$-Ni(100) spectrum is broad enough that a high frequency component could be present.

Another possible fragment which could produce the 795 $cm^{-1}$ loss is a $CH_2$ species. The 795 $cm^{-1}$ peak is only slightly higher in frequency than a CH bend from a methylene group (typically around 740 $cm^{-1}$) and only slightly lower than a $CH_2$ deformation (at 850 $cm^{-1}$). If a $CH_2$ species is present, the $CH_2$ scissor mode, expected at ~1400 $cm^{-1}$ would be obscured by the peak ascribed to the methyl deformations. It would also be difficult to observe the $CH_2$ rock in the presence of a $CH_3$ rock. A final possibility, which will be discussed in section C, would attribute the 795 $cm^{-1}$ peak to surface hydrogen.

The most intense peak in the $CH_3N_2CH_3$-Ni(100) spectrum, at approximately 1066 $cm^{-1}$, best corresponds to methyl rocking modes ($\nu_{11}$ at ~1026 $cm^{-1}$ or $\nu_{15}$ at ~1112 $cm^{-1}$) of gas-phase azomethane. This peak is observed to have a fairly strong impact contribution. The broad peak centered at 1408 $cm^{-1}$ is attributed to the methyl deformations, although the presence or absence of any individual deformation mode cannot be determined. Like the peak at 1066 $cm^{-1}$, the 1408 $cm^{-1}$ peak is observed to nave a strong impact

contribution (Figs. 1 and 2). In both of these assignments, agreement with the corresponding modes of free azomethane is quite good, as is agreement with the methyl rocks and deformations of similar adsorbates on Ni(111) and Rh(111).

Friend et al.[31] ascribed an intense peak at 1400 $cm^{-1}$ in the vibrational spectrum of acetonitrile, $CH_3CN$, weakly adsorbed on Ni(111) to a methyl deformation and a peak at 1020 $cm^{-1}$ to a methyl rock. In the vibrational spectrum of methyl isocyanide, $CH_3NC$, which chemisorbs strongly on Ni(111) at 300 K, they observed peaks at 1480 and 1400 $cm^{-1}$ which they attributed to methyl deformations. They also observed an intense peak at 1100 $cm^{-1}$, although they did not explicitly assign this peak. Semancik et al.[30] assigned a peak at 1430 $cm^{-1}$ in the spectrum of methyl isocyanide on Rh(111) to a methyl deformation. The agreement among the vibrational frequencies of the methyl deformation and rocking modes from several different systems supports the assignments made above.

The intense peak at 1150 $cm^{-1}$ probably corresponds to a C-N stretch. This frequency is close to that observed in the Raman spectra of gas- and solid-phase azomethane[40-42] or the symmetric C-N stretch (1180 $cm^{-1}$). Semancik et al.[30] observed a C-N stretch at 1120 $cm^{-1}$ for $CH_3NC$ adsorbed in a 3-fold site on Rh(111) at 120 K. A low intensity peak at ~1012 $cm^{-1}$ in the $CH_3N_2CH_3$-Ni(100) spectra is extremely difficult to isolate from the very intense peak at 1066 $cm^{-1}$, but it does appear as a shoulder on this peak in the majority of the spectra. It can be attributed to a number of modes -

a CNN bend, a methyl rock, or the asymmetric C-N stretch.

The peak at 1640 $cm^{-1}$ can be attributed to a N=N stretch, with an upward frequency shift of about 60 $cm^{-1}$ from the gas-phase value of 1580 $cm^{-1}$. Table 3 lists the N=N stretching frequencies of some organometallic complexes containing ligands which coordinate to one or more metal centers through an azo linkage. In almost every complex, the N=N stretching frequency shifts down from the gas-phase value. When upward shifts are observed, the shift is only about 20 $cm^{-1}$, but in all of these complexes the azo functional group is coordinated to only one metal atom through a N lone pair.

The CH stretch region in the $CH_3N_2CH_3$-Ni(100) off-specular spectrum is broad and asymmetric. The symmetric $CH_3$ stretches are centered at 2920 $cm^{-1}$ and the asymmetric stretches at 2985 $cm^{-1}$. There is sufficient intensity in the 2950-3000 $cm^{-1}$ region to indicate the presence of some $sp^2$ hybridized C, although the most intense part of the band corresponds to $sp^3$ hybridized carbon. A CH or $CH_2$ surface species or $CH_2$ on the adsorbate complex (formed by CH bond scission) could all involve $sp^2$ hybridized carbon. The shoulder at 2780 $cm^{-1}$ is believed to correspond to a softened $CH_3$ vibrational mode. Several examples of this effect have been reported in the literature.[2,52,53]

Demuth et al. reported a softened C-H stretch at 2730 $cm^{-1}$, shifted 240 $cm^{-1}$ down from the normal $CH_2$ stretching frequency (2970 $cm^{-1}$), for ethylene adsorbed on Ni(111) and attributed it to a hydrogen bond-like electronic interaction between some of the hydrogen

atoms and the surface.[53] They proposed that such bonding preceded CH bond scission - ethylene on Ni(111) decomposed into $C_2H_2$ and $H_2$ at ~230 K. They did not observe mode softening for the $C_2H_4$-Pt(111) system, nor did they observe any evidence of CH bond scission.[54] Gates and Kesmodel reported a softened C-H mode for ethylene adsorbed on Pd(111), and, although the magnitude of the shift was not as large
as that reported by Demuth et al., they also attributed the mode softening to C-H-M multicenter interactions.[2]

In summary, the following features are observed in the $CH_3N_2CH_3$-Ni(100) spectra:

1) The intensity of the carbon-metal stretch at 329 $cm^{-1}$ indicates that some dissociation of the azomethane occurs on Ni(100) at 300 K.

2) Seven of the remaining eight peaks in the spectrum can be attributed to molecular $CH_3N_2CH_3$, although in one case (530 $cm^{-1}$ loss) the assignment is somewhat ambiguous. The very weak feature at 530 $cm^{-1}$ can be attributed to either a CNN bend or a N-Ni stretch. The peak at 795 $cm^{-1}$ may result from a $CH_3$ rock, a CH or $CH_2$ surface species, or from a $CH_2$ group formed by C-H bond cleavage at one of the azomethane C-H bonds. It could also indicate the presence of surface hydrogen. If a $CH_3$ rock is responsible for the loss, the large shift from the gas-phase frequency suggests that this mode is strongly perturbed by

adsorption on the Ni(100) surface. None of the other $CH_3$ modes seem to be significantly perturbed, however, implying that this assignment is incorrect.

3) The presence of any appreciable quantity of molecular azomethane makes the identification of coadsorbed fragmentation products difficult. The most likely candidates are a CH surface species (795 $cm^{-1}$ peak) or a $CH_2$ species, present on the surface or formed on the azomethane by CH bond scission (1408 and 795 $cm^{-1}$ peaks, asymmetry of CH stretching region). Carbon is clearly present on the surface, but the presence or absence of atomic nitrogen and hydrogen cannot be established from the 300 K $CH_3N_2CH_3$-Ni(100) spectra.

4) The shoulder at 2770 $cm^{-1}$ on the CH stretch band in the off-specular $CH_3N_2CH_3$-Ni(100) spectrum indicates that mode softening is occurring. In other systems where it is observed, mode softening results from a multicenter interaction between methyl or methylene hydrogens and a metal surface. This interaction is proposed to precede CH bond scission.[53]

5) The large intensity and the high frequency of the peak attributed to the N=N stretch are inconsistent with a geometry in which the N=N bond is parallel with the surface. The loss associated with the N=N stretch would be expected to be of low intensity if the N=N

bond vector was parallel or near parallel with the surface. By analogy with the inorganic complexes in Table 3, the high frequency suggests that the azomethane is coordinated to a single Ni surface atom, through a N lone pair. Hence, the $CH_3N_2CH_3$-Ni(100) system at 300 K does not display the characteristics expected for a $\pi$-bonded system, although the adsorbate-surface interaction is somewhat stronger than that expected for interaction solely through the N lone pair. The enhanced interaction may result from the geometry of the azomethane molecule. When it adsorbs on the flat Ni(100) surface through a nitrogen lone pair, some of the methyl hydrogens are in close enough proximity to the surface that C-H-Ni multicenter bonds can form.

6) Both the energy loss and the Auger spectra indicate that the saturation coverage of azomethane on Ni(100) is one monolayer or less.

3. Annealed Spectra of $CH_3N_2CH_3$-Ni(100).

In addition to the spectra of $CH_3N_2CH_3$ adsorbed on Ni(100) at room temperature, spectra were taken of $CH_3N_2CH_3$ adsorbed at room temperature and then annealed briefly to a higher temperature. These spectra are shown in Figure 3. The annealing temperatures ranged from 375 to 425 K. The four spectra taken after such anneals are quite different from the "room temperature" spectra and indicate that a surface reaction occurs at the elevated temperatures.

The most striking feature of the "annealed spectra" is the appearance of a new and very intense peak at 970 $cm^{-1}$, shifting up to 980 $cm^{-1}$ by the 425 K anneal. Furthermore, as this feature grows in, the two most intense features of the room temperature spectra, the peaks at 1066 and 1152 $cm^{-1}$, lose intensity. After anneals at 400 and 425 K, these peaks are reduced to a shoulder on the peak at 980 $cm^{-1}$. The 1152 $cm^{-1}$ peak retains some intensity in the spectrum taken after the 425 K anneal.

The very weak feature at 530 $cm^{-1}$ in the room temperature Ni(100) spectra cannot be observed in any of the annealed spectra. The peak at 795 $cm^{-1}$ broadens considerably after the 375 K anneal and cannot be picked out of the background after a 385 K anneal. In all of the annealed spectra, the background between 500 and 800 $cm^{-1}$ is very high and uneven. The broad, room temperature peak at 1408 $cm^{-1}$ shifts to 1396 $cm^{-1}$ after the 375 K anneal and is present in all the annealed spectra, although there seems to be a dispersion of about 10 $cm^{-1}$ in its location. The 1640 $cm^{-1}$ peak is broadened by each anneal and ultimately seems to split into at least two peaks. Finally, after the 425 K anneal, a low intensity peak appears at 1545 $cm^{-1}$. The CH stretching region maintains some intensity after the 375 and 385 K anneals. The lack of any intensity in this region after the two higher temperature anneals cannot, however, be taken as evidence that there are no longer any $CH_x$ moities on the surface.

A comparison of the annealed and room temperature spectra suggests a possible dissociation model for $CH_3N_2CH_3$ on Ni(100),

which we will now describe. Assuming that azomethane adsorbs molecularly, for the most part, on Ni(100) at room temperature and using the assignments in Table 2, the disappearance of the intense peaks at 1066 and 1152 $cm^{-1}$ upon annealing can be taken as evidence of CH and CN bond cleavage. The fragments may stabilize, for example, as surface H and surface $CH_2$ species. The mode softening observed in the off-specular, room temperature spectrum indicates that one or more CH bonds are significantly perturbed following adsorption of the azomethane on the Ni(100) surface, while the CN bond is relatively undisturbed. Once a CH bond has been broken, however, the CN bond may be significantly more activated to bond cleavage. The very intense feature at 970-980 $cm^{-1}$ in the annealed spectra could correspond to a $CH_2$ wag, and the peak at approximately 1410 $cm^{-1}$, attributed to a $CH_3$ deformation in the room temperature spectra, could be attributed to a $CH_2$ scissor mode. Such assignments are supported by the results of other workers. George et al.[29] observed fairly intense features at 970 and 1422 $cm^{-1}$ for the $CH_2N_2$-Ru(001) system and attributed them to the $CH_2$ wag and the $CH_2$ scissor mode, respectively, of a $CH_2$ surface species. They also observed a $CH_2$ rock at 1135 $cm^{-1}$, for which the $CH_3N_2CH_3$-Ni(100) system has no analogue, unless it is obscured by the shoulder of the 970-980 $cm^{-1}$ loss peak. Demuth et al.[12] observed the formation of a $CH_2$ surface species on Ni(111) at 450 K and above, from the decomposition of acetylene. This species exhibited loss features at 790, 1300, and 2980 $cm^{-1}$ ($CH_2$ bend, scissor, and stretch, respectively).

The rapid disappearance of the 1066 and 1152 $cm^{-1}$ peaks in the $CH_3N_2CH_3$-Ni(100) spectra upon annealing implies that both CN bonds of the azomethane are broken and that both methyl groups fragment, although it seems likely that one methyl group would be more "activated" for dissociation than the other. If only one CN bond breaks, the orientation of the second CN bond and the second methyl group on the remaining fragment may be such that the dynamic dipole of the CN stretch and the methyl rock are imaged in the metal surface, making observation of the corresponding losses difficult. The remaining CN bond could be parallel or near parallel with the surface, for example. Or, the dynamic dipole for the $CH_3$ stretch and the CN stretch may be small in magnitude, resulting in near zero intensity for the corresponding losses.

If one or both CN bonds of the azomethane breaks, the fragment containing the two nitrogen atoms could orient with its N=N bond parallel to the surface. Such a configuration was proposed for the $N_2$/Fe(111) system by Grunze et al.[33] who reported a decrease in the N≡N stretching frequency from its gas-phase value of 2331 $cm^{-1}$ to 1490 $cm^{-1}$ when it was adsorbed on the Fe(111) surface at 110 K. A side-on configuration of the azomethane would allow the N=N $\pi$-electron system, as well as both nitrogen lone pairs, to overlap efficiently with the metal surface. In this model, the $\pi^*$ orbital of the azo function acts as an electron acceptor. Bonding would initially occur by donation of electron density from the $\pi$-orbital and from the N lone pairs of the azo linkage to the metal, followed by

back-bonding from the metal d orbitals to the $\pi^*$ orbitals of the chemisorbed azomethane. Such bonding would increase the strength of the adsorbate-surface bond, but partial occupation of the $\pi^*$ orbital of azomethane would decrease the N=N bond strength and therefore the NN stretching frequency. $\pi$ bonding through the azo linkage has been observed in some Fe-containing organometallics with diazene ligands.[24,25,47,48]

This arrangement, in which the N=N bond is parallel to the surface, could also occur if the trans-azomethane isomerizes to the cis form. Conversion to the cis isomer is unlikely, however. It is much less stable than the trans isomer, and, once formed, tautomerizes easily to $CH_2NNHCH_3$. In cis-azomethane, there is severe crowding of the two methyl groups, due to the short N=N bond distance.[55] (The structural parameters of the cis form are approximately the same as those of the trans isomer.) If $CH_2NNHCH_3$ were present on the surface, several new stretching modes, which are inconsistent with the spectra, would be expected. The N=N stretch would be replaced by a N-N stretch at ~950 $cm^{-1}$. Two different CN bond stretches, one at ~1650 $cm^{-1}$ for the C=N and one at ~1200 $cm^{-1}$ for the C-N, would be expected. Finally, an NH stretch at ~3200 $cm^{-1}$ would also be expected. Hence, CH and CN bond scission seems a more likely route for the dissociation of azomethane observed at elevated temperatures than does its conversion to the cis isomer, followed by tautomerization and N-N bond cleavage.

The spectra do not contain any evidence for $\pi$ bonding between the

azo linkage and the Ni(100) surface, even after the sample has been annealed. The observed increase in the N=N stretching frequency over the gas-phase frequency, for both the annealed $CH_3N_2CH_3$-Ni(100) surfaces and those maintained at 300 K, is inconsistent with an adsorption geometry in which the N=N bond is parallel or near parallel with the surface. If the azo function were interacting with the Ni(100) surface through its $\pi$-electron system, decreases in the frequency and in the intensity of the peak attributed to the N=N stretch would be expected. The intensity and frequency of the loss peak attributed to the N=N stretch are strong evidence that the azomethane bonds to the Ni(100) surface through a nitrogen lone pair. CN bond cleavage may cause partial rehybridization of the azo linkage. This could explain the upward shift observed for the peak attributed to the N=N stretch, especially after annealing.

Finally, the disappearance of the 795 $cm^{-1}$ peak after annealing the $CH_3N_2CH_3$ surface to 385 K is inconsistent with the stability of the CH surface species observed on Ni(111) between 300 and 450 K.[12] It is also inconsistent with the stability of the $CH_2$ surface species observed on the same surface. Hydrogen desorbs from the Ni(111) surface at ~390 K, however, and could be responsible for this loss.[32]

Friend et al.[32] studied the $CH_3NC$-Ni(111), $CH_3NC$-Ni(111)-C, $CH_3NC$-Ni(100), and $CH_3NC$-Ni(100)-C systems using thermal desorption. They found that $CH_3NC$ chemisorbed strongly and irreversibly to the Ni(100) and Ni(111) surfaces at 300 K and

decomposed to form $H_2$, HCN, and $N_2$ at elevated temperatures. In contrast, on the Ni(100)-C and Ni(111)-C surfaces, $CH_3NC$ chemisorbed and then isomerized to $CH_3CN$ during the thermal desorption experiment. Using isotopic labeling studies, they demonstrated that the $CH_3NC$-to-$CH_3CN$ isomerization on the carbon-containing surfaces was intramolecular and that the carbon atom source for the carbon in the HCN which desorbed from the $CH_3NC$-Ni surfaces was the methyl carbon in the $CH_3NC$. The desorption temperatures of HCN, $H_2$, and $N_2$ from the $CH_3NC$-Ni(111) surface observed in this work were 490 K, 390 K, and 770 K, respectively. HCN desorbed at 465 K, $H_2$ at 475 K, and $N_2$ at 770 K from the $CH_3NC$-Ni(100) surface.

On the clean surfaces, Friend et al. postulated that the NC vector of $CH_3NC$ was parallel or near parallel with the surface and that both the isocyanide carbon and nitrogen atoms were within bonding distance of the surface metal atoms. Such a geometry would allow the methyl hydrogen atoms close enough to the surface to permit facile CH bond scission, which they proposed as the initial decomposition process on these surfaces. A later vibrational study[31] of the $CH_3NC$-Ni(111) and $CH_3NC$-Ni(111)-C surfaces could not determine if the NC bond vector was parallel to the nickel surface with both the carbon and nitrogen atoms bonded to the surface or if the NC bond vector was normal to the surface with the carbon atom bridge-bonded to two or three nickel atoms.

Several conclusions can be drawn from the comparison of the spectra of $CH_3N_2CH_3$ adsorbed on Ni(100) and maintained at room

temperature and those of the annealed surfaces. The room temperature model of initial bonding to the surface by donation of one of the nitrogen lone electron pairs can explain the room temperature spectra, if some dissociation is assumed. As soon as the surface temperature increases, CH and CN bond scission occur at observable rates. One of the dissociation products may be a $CH_2$ species, either on the surface or replacing one of the methyl groups of the azomethane. Another dissociation product is hydrogen, which may be responsible for the 795 $cm^{-1}$ loss at 300 K and which desorbs at elevated temperatures. Finally, at elevated temperatures, as at room temperature, the azomethane interacts with the Ni(100) surface through one of the nitrogen lone pairs.

4. $CH_3N_2CH_3$-Ni(111)

The spectrum of azomethane on Ni(111), taken in the specular direction, is shown in Figure 4. This spectrum will not be discussed in detail, but some plausible assignments will be suggested. The spectrum is quite different from that of $CH_3N_2CH_3$-Ni(100). Even if the adsorbed species were the same on both surfaces, some differences in the vibrational frequencies of given "internal" modes would be expected, because of the different geometric structure and electronic properties of each surface. The energy loss spectra of azomethane adsorbed on the two Ni surfaces at 300 K are, however, quite distinct and imply that azomethane interacts differently with the two surfaces.

The carbon-nickel stretch appears at 448 $cm^{-1}$ in the Ni(111) spectra as a shoulder on the elastic peak. There are two other low frequency losses, at 750 and 850 $cm^{-1}$, in the Ni(111) spectrum. The 750 $cm^{-1}$ peak occurs 45 $cm^{-1}$ too low to correspond with the frequency attributed to the bending mode of the CH surface species formed by the decomposition of acetylene on Ni(111).[12] It could be assigned to a H-Ni stretch or a methyl rock. The low intensity peak at 850 $cm^{-1}$ could result from $CH_2$ modes, a $CH_2$ deformation or a $CH_2$ wag. Acetylene chemisorbed on Ni(111) at 300 K[12] exhibits a $CH_2$ deformation at 875 $cm^{-1}$, and the $CH_2$ wag of the $(CH_2)$ surface species on Ru(001)[29] occurs at 970 $cm^{-1}$. These assignments imply that, at 300 K, the Ni(111) surface is slightly more reactive with respect to azomethane than the Ni(100) surface. The most intense peak in the Ni(111) spectrum, at 1059 $cm^{-1}$, was assigned by analogy to the gas-phase spectrum to a methyl rock. This peak is broad and asymmetric and is almost certainly composed of overlapping losses. An asymmetric shoulder at 993 $cm^{-1}$ can be ascribed to either another methyl rock or the asymmetric CN stretch.

The broad feature between 1220 and 1295 $cm^{-1}$ probably consists of two superimposed features; both could be attributed to normal modes of a $CH_2$ or $CH_3$ group, or the 1220 $cm^{-1}$ peak could be ascribed to a strongly perturbed CN symmetric stretch. The peak at 1413 $cm^{-1}$ is attributed to a $CH_3$ mode and that at 1493 $cm^{-1}$ to the N=N stretch, shifted down from its gas-phase value by about 80 $cm^{-1}$. There is no intensity in the CH stretching region of the Ni(111)

spectra, although $CH_3$ and/or $CH_2$ groups must be responsible for many of the low energy peaks in the spectrum. The absence of any features in the CH stretch region is attributed to unfavorable magnitudes and orientations of the dynamic dipoles for these modes.

There are not enough data on the $CH_3N_2CH_3$-Ni(111) system to make many definitive assignments of the spectrum. The frequency shifts observed for the adsorbed species indicate that the azomethane is strongly perturbed from its gas- (and solid-) state by adsorption on the Ni(111) surface. The variation in the frequencies of the losses ascribed to the N=N stretch on the Ni(100) and Ni(111) surfaces suggests that the azomethane-substrate interaction is different in the two cases. The azo linkage may partially interact with the Ni(111) surface through its $\pi$-electron system, weakening the N=N bond and causing a reduction in the frequency at which the N=N stretch occurs. The magnitude of the downward shift in the N=N stretching frequency from the gas-phase frequency is not that great, however. Furthermore, the Ni(100) plane, with exposed atoms of coordination number 8, should be a better electron donor plane than the Ni(111) plane, with exposed atoms of coordination number 9, but the N=N stretching frequency increases when azomethane is adsorbed on Ni(100). A more likely explanation for the different N=N stretching frequencies on the two nickel surfaces invokes adsorption at different sites. The azomethane may bond to the Ni(111) surface through its nitrogen lone pair, as on Ni(100), but at a 2-fold or 3-fold site, not at an atop site. A decrease in the N=N stretching frequency under these circumstances

would not be surprising.

The appearance of a loss feature which can be ascribed to a H-Ni stretch and the intensity of the C-Ni loss indicate that some decomposition of the azomethane occurs on Ni(111) at 300 K. The initial step in this decomposition is probably CH bond scission at the C-H-Ni multicenter bonds. It is difficult to determine if C-N bond cleavage is complete on the Ni(111) surface at 300 K due to the complexity of the spectrum in the 900-1500 $cm^{-1}$ region. The spectrum can be adequately explained by a mixture of decomposition products, but the presence of some molecular azomethane cannot be ruled out.

5. $CH_3N_2CH_3$ on Cr(100) and Cr(111).

The energy loss spectra of azomethane adsorbed on Cr(100) (specular and off-specular) and Cr(111) (specular) are shown in Figures 5 and 6. Again, the spectra shown are for saturation coverage at room temperature. As with the Ni(100) spectra, there are differences in the relative intensities of some of the peaks in the Cr(100) spectra taken in the specular and off-specular directions. A feature at 805 $cm^{-1}$ in the off-specular spectrum is not present at all in spectra taken in the specular direction. Hence, the species responsible for the loss is assumed to have a symmetry higher than $C_1$.

The peak at 925 $cm^{-1}$ is fairly intense in the specular direction but appears only weakly in the off-specular direction. This

peak can be ascribed to either a C-N stretch or a $CH_3$ rock. The most intense feature in both the specular and off-specular Cr(100) spectra is a peak at 1034-1044 $cm^{-1}$. By analogy with the Ni(100) spectra, this peak could be assigned to a methyl rock. There is a broad band between 1170 and 1260 $cm^{-1}$ in both spectra which probably consists of at least two unresolved peaks. Both could be attributed to $CH_2$ or $CH_3$ modes, or one of them could be attributed to a C-N stretch. A peak at ~1440 $cm^{-1}$ is observed to have a strong impact contribution as was the 1408 $cm^{-1}$ peak on the Ni(100) surface and, like that peak, is attributed to a $CH_3$ deformation. Tailing on the high frequency side of the 1440 $cm^{-1}$ peak in both Cr(100) spectra could represent a low intensity loss centered at about 1590 $cm^{-1}$, which corresponds well with the gas-phase N=N stretching frequency. The low (near zero) intensity of the spectrum in the region of the expected N=N stretching frequency indicates that either the N=N bond is parallel with the surface or that the azomethane has decomposed, with N=N bond cleavage.

There is little intensity in the CH stretch region of the Cr(100) spectrum taken in the specular direction, but off-specular measurements do indicate the presence of $CH_x$ species. Furthermore, as in the Ni(100) spectra, there is evidence for mode softening in the CH stretch on the Cr(100) surface. The Cr(100) spectra show a very intense peak at ~515 $cm^{-1}$ which was assigned to the carbon-chromium stretch by comparison with the spectra of $CO^{34}$ and $CH_3NH_2^{18}$ adsorbed on Cr(100) at 300 K. The intensity of the carbon-chromium

stretch indicates that a substantial quantity of azomethane has dissociated. The Cr-N stretch occurs at 560 $cm^{-1}$.[18] It is very weak, however, and cannot be seen in the presence of an intense Cr-C stretch. A shoulder on the C-Cr peak, at 657 $cm^{-1}$, in both the specular and off-specular Cr(100) spectra is not assigned. Either this loss or that at 805 $cm^{-1}$ could be attributed to a H-Cr stretch.

The complexity of the spectra and the ambiguity in the assignments make it impossible to determine if complete dissociation of the azomethane has occurred. $CH_3$ and/or $CH_2$ species are present as indicated by the losses ascribed to methyl deformation and rock modes, and the shoulder on the low frequency side of the CH stretch band suggests that CH bond weakening occurs on the Cr(100) surface. The absence of a definite loss for the N=N stretch could result from the orientation of the N=N bond vector, or, more likely, from N=N bond cleavage. On the Cr(100) surface, the N=N bond does not necessarily have to be parallel with the surface for efficient overlap between the $\pi$ orbitals of the azo linkage and the d orbitals of the metal surface atoms. An effective side-on bonding geometry is possible, even if the initial adsorption occurs through a nitrogen lone pair. If N=N bond cleavage occurs, species such as $H_2CN$ or $H_3CN$ may exist on the surface. Decomposition products containing cyano functions can probably be ruled out, at least in the room temperature spectra. The CN stretch in free HCN[56] occurs at ~2100 $cm^{-1}$, and there is no evidence of even a weakened CN stretch in the $CH_3N_2CH_3$-Cr(100) spectra.

The $CH_3N_2CH_3$-Cr(111) spectrum is the simplest in appearance of all the $CH_3N_2CH_3$ surface spectra. A very broad peak, centered at about 417 $cm^{-1}$, cannot be completely resolved from the elastic peak. This loss is assigned to the C-Cr stretch by comparison with the spectra of CO and $CH_3NH_2$ on Cr(111), and its intensity indicates that dissociation of $CH_3N_2CH_3$ occurs on the Cr(111) surface at 300 K.[18,34] The N-Cr stretch on Cr(111) has not been assigned, but it is likely that it would be obscured by the intensity of the C-Cr loss peak. There are three broad and intense losses in the spectrum which correspond well with frequencies of normal modes of $CH_3/CH_2$ groups. The loss at 1077 $cm^{-1}$ agrees well with the methyl rocks of gas-phase azomethane and that at 1419 $cm^{-1}$ with the methyl deformations of gas-phase azomethane. The $CH_2$ surface species on Ru(001) exhibited a scissor mode at 1422 $cm^{-1}$, a $CH_2$ rock at 1135 $cm^{-1}$, and a $CH_2$ wag at 970 $cm^{-1}$. The asymmetry on the low frequency side of the 1077 $cm^{-1}$ peak and that on the high frequency side of the 1419 $cm^{-1}$ peak may result from unresolved losses, for example a CN stretch at ~1000 $cm^{-1}$ and a N=N stretch at ~1500 $cm^{-1}$. They could also result from $CH_3$ or $CH_2$ modes. The asymmetry of the CH stretch band between 2760 $cm^{-1}$ and 3000 $cm^{-1}$ is indicative of mode softening, and its broadness indicates that $sp^2$ as well as $sp^3$ hybridized carbon atoms are present. A very low intensity loss centered at ~3285 $cm^{-1}$ could correspond to an NH stretch or a CH stretch for an sp hybridized carbon. The spectrum is strong evidence for essentially complete decomposition of the

azomethane. Given the absence of any real losses which can be assigned to a N=N stretch or a CN stretch, we conclude that $CH_2$, $CH_2N$, or $CH_3N$ surface species are the most likely candidates for fragmentation products, in addition to atomic hydrogen, carbon, and nitrogen.

D. Conclusion

A saturation coverage of $CH_3N_2CH_3$ was studied on the (100) and (111) surfaces of Ni and Cr at 300 K using EELS. A correlation of the surface frequencies to those of gaseous and solid azomethane and organometallic complexes was used to assign the vibrational losses of the chemisorbed species at 300 K. Molecular $CH_3N_2CH_3$ bonded through the nitrogen lone pair was identified on Ni(100) at 300 K. Seven of the nine loss peaks in the $CH_3N_2CH_3$-Ni(100) spectrum can account for many modes of gas-phase azomethane. Furthermore, the high frequency of the loss attributed to the N=N stretch supports a model in which the adsorbed $CH_3N_2CH_3$ bonds to the nickel surface through a nitrogen lone pair. If the $CH_3N_2CH_3$ bonded to the surface through its $\pi$ orbitals, a reduction in the N=N or C-N stretching frequency would be expected. The geometry of the azomethane-surface complex allows formation of a three-centered C-H-Ni bond which significantly weakens the CH bond and lowers the activation barrier to dissociation.

The energy loss spectra of the annealed $CH_3N_2CH_3$-Ni(100) surfaces indicate the formation of at least one and perhaps two

hydrocarbon phases which are significantly different from that observed on the surfaces maintained at room temperature. The most likely initial step in the thermal decomposition of $CH_3N_2CH_3$ on Ni(100) is CH bond cleavage, followed by CN bond cleavage. Possible decomposition products include, besides adsorbed carbon, hydrogen, and nitrogen, $CH_xN$-Ni, as well as CH and $CH_2$ surface species.

The $CH_3N_2CH_3$-Ni(111) spectrum suggests that some dissociative adsorption occurs on this surface at 300 K, but the extent of the dissociation cannot be determined in the presence of molecular azomethane. Fragments such as CH, $CH_2$, $NCH_3$, and $CNCH_x$ cannot be easily distinguished from $CH_3N_2CH_3$ using EELS. If the azomethane bonds to the nickel surfaces by donation of a nitrogen lone electron pair, increased decomposition relative to the $CH_3N_2CH_3$-Ni(100) system might be expected, because the Ni(111) plane should serve as a better electron acceptor plane than the Ni(100) plane. The decrease in the N=N stretching frequency of azomethane adsorbed on the Ni(111) plane relative to that of both the free molecule and azomethane adsorbed on the Ni(100) plane suggest that the adsorption site is a bridge or 3-fold hollow on Ni(111) and an atop site on Ni(100).

Extensive or complete decomposition of the azomethane to fragments such as $CH_2$, $CH_3$, $NCH_2$, and $NCH_3$ is believed to occur on the Cr(100) and Cr(111) surfaces at 300 K. $NH_x$ species may also be present on the Cr(111) surface. A comparison of the spectra of $CH_3N_2CH_3$ on the nickel and chromium surfaces suggests that

the adsorbate-substrate interaction is different on the two metals. The most striking difference between the spectra of azomethane adsorbed on the nickel and chromium surfaces is the absence, in the Cr spectra, of a clear-cut loss which can be attributed to a N=N stretch. This probably indicates that extensive N=N bond cleavage has occurred. The structure of both chromium surfaces is sufficiently open that the N=N bond would not have to be parallel with the surface plane for favorable overlap between the chromium d orbitals and the $\pi$ orbitals of the azo linkage. Bonding via the $\pi$ orbitals of the azomethane is sterically difficult to achieve on the flatter nickel surfaces because of the bulky geometry of the azomethane adsorbate.

In the adsorption of $CH_3N_2CH_3$ on nickel, the surface functions as an electron acceptor; bonding occurs via donation of electron density from the nitrogen lone pair of the azomethane. The same type of interaction is observed in the adsorption of CO and $CH_3NH_2$ on nickel at room temperature. Some electron donation from the nickel surface to the $\pi^*$ orbital of CO does occur, but at 300 K it is not extensive enough to cause dissociation of the CO. On the other hand, the Cr surfaces function primarily as electron donors. Both $CH_3N_2CH_3$ and CO have empty orbitals of suitable symmetry to which the Cr surface atoms can contribute electron density. This strengthens the adsorbate-surface bond but weakens the internal bonding of the adsorbate, leading to dissociation. When CO or $CH_3N_2CH_3$ is adsorbed on Cr(100) or Cr(111), no undissociated species exist on either surface at 300 K. No suitable orbitals are

available in $CH_3NH_2$ to accept electron density from the metal surface, however, so bonding occurs via donation of electron density from the nitrogen lone pair on the $CH_3NH_2$ to the metal surface. The interaction of $CH_3NH_2$ with the chromium surfaces is weaker than that of $CH_3N_2CH_3$. For example, carbon or nitrogen atoms of initially dissociated $CH_3NH_2$ can partially passivate the chromium surfaces and allow subsequent molecular adsorption.[18] Atomic adsorbates, acting as electron donors, should tend to increase the electron density of surface metal atoms and weaken the interaction between the surface and an electron-donating adsorbate. The frequencies of the internal modes of $CH_3NH_2$ adsorbed on a carbon or nitrogen covered chromium surface are only slightly perturbed from their gas-phase values. On the other hand, the frequencies of the losses observed for azomethane following adsorption on the Cr(100) or (111) surfaces are strongly perturbed from the gas-phase values and indicate that the adsorbate-substrate interaction is very strong. Furthermore, there is no evidence that initially dissociated $CH_3N_2CH_3$ can passivate the Cr(100) and Cr(111) surfaces, allowing subsequent molecular adsorption at 300 K.

## References


* This chapter is based on experiments performed in collaboration with A.G. Baca and D.A. Shirley.

1. H. Ibach and D.L. Mills, Electron Energy Loss Spectroscopy and Surface Vibrations (Academic Press, New York, 1982).
2. J.A. Gates and L.L. Kesmodel, Surf. Sci., 120, L461 (1982).
3. H. Ibach, H. Hopster, and B. Sexton, Appl. Phys., 14, 21 (1977).
4. H. Ibach and S. Lehwald, J. Vac. Sci. Technol., 15, 407 (1978).
5. J.E. Demuth and H. Ibach, Surf. Sci., 85, 365 (1979).
6. C. Backx and R.F. Willis, Chem. Phys. Lett., 53, 471 (1978).
7. L.H. Dubois, D.G. Castner, and G.A. Somorjai, J. Chem. Phys., 72, 5234 (1980).
8. L.L. Kesmodel, L.H. Dubois, and G.A. Somorjai, Chem. Phys. Lett., 56, 267 (1978).
9. L.L. Kesmodel, L.H. Dubois, and G.A. Somorjai, J. Chem. Phys., 70(5), 2180 (1979).
10. M.-C. Tsai, C.M. Friend, and E.L. Muetterties, J. Am. Chem. Soc., 104, 2539 (1982).
11. C.M. Friend and E.L. Muetterties, J. Am. Chem. Soc., 103, 773 (1981).
12. J.E. Demuth and H. Ibach, Surf. Sci., 78, L238 (1978).
13. S. Lehwald and H. Ibach, Surf. Sci., 89, 425 (1979).
14. G. Broden, T.N. Rhodin, C. Brucker, R. Benbow, and Z. Hurych, Surf. Sci., 59, 593 (1976).

15. G.B. Fisher and G.E. Mitchell, J. Electron Spectrosc. Related Ph., 29, 253 (1983).

16. B. Sexton and G.E. Mitchell, Surf. Sci., 99, 523 (1980).

17. B. Sexton, Surf. Sci., 88, 299 (1979).

18. A.G. Baca, M.A. Schulz, and D.A. Shirley, J. Chem. Phys., XX, XXXX (1985).

19. R.M. Wexler, M.-C. Tsai, C.M. Friend, and E.L. Muetterties, J. Am. Chem. Soc., 104, 2034 (1982).

20. R.M. Wexler and E.L. Muetterties, J. Am. Chem. Soc., 106, 4810 (1984).

21. Ph. Avouris and J.E. Demuth, J. Chem. Phys., 75(10), 4783 (1981).

22. N.J. DiNardo, Ph. Avouris, and J.E. Demuth, J. Chem. Phys., 81(4), 2169 (1984).

23. M.N. Ackermann, D.J. Dobmeyer, and L.C. Hardy, J. Organomet. Chem., 182, 561 (1979).

24. R.S. Dickson and J.A. Ibers, J. Am. Chem. Soc., 94(9), 2988 (1972).

25. R.J. Doedens and J.A. Ibers, Inorg. Chem., 8(12), 2709 (1969).

26. M.N. Ackermann, L.-J. Kou, J.M. Richter, and R.M. Willett, Inorg. Chem., 16(6), 1298 (1977).

27. M.N. Ackermann and L.-J. Kou, J. Organmet. Chem., 86, C7 (1975).

28. D. Sellmann, A. Brandl, and R. Endell, J. Organomet. Chem., 111, 303 (1976).

29. P.M. George, N.R. Avery, and W.H. Weinberg, J. Am. Chem. Soc., 105, 1393 (1983).

30. S. Semancik, G.L. Haller, and J.T. Yates, Jr., J. Chem. Phys., 78 (11), 6970 (1983).

31. C.M. Friend, E.L. Muetterties, and J.L. Gland, J. Phys. Chem., 85, 3256 (1981).

32. C.M. Friend, J. Stein, and E.L. Muetterties, J. Am. Chem. Soc., 103, 767 (1981).

33. M. Grunze, M. Golze, W. Hirschwald, H.-J. Freund, H. Pulm, U. Seip, M.-C. Tsai, G. Ertl, and J. Kuppers, Phys. Rev. Lett., 53(8), 850 (1984).

34. A.G. Baca, L.E. Klebanoff, M.A. Schulz, E. Paparazzo, and D.A. Shirley, to be submitted to Surf. Sci.

35. H. Kato, Y. Sakisaka, T. Miyano, K. Kamei, M. Nishijima, and M. Onchi, Surf. Sci., 114, 96 (1982).

36. Z. Murayama, E. Kojima, E. Miyazaki, and I. Yasumore, Surf. Sci., 118, L281 (1982).

37. E.G. Keim, F. Labohm, O.L.J. Gijzeman, G.A. Bootsma, and J.W. Geus, Surf. Sci., 112, 52 (1981).

38. D.H. Rosenblatt, Ph.D. thesis, University of California, Berkeley, 1982 (LBL-14774, unpublished).

39. R. Renaud and L.C. Leitch, Can. J. Chem., 32, 549 (1954).

40. J.R. Durig, C.B. Pate, and W.C. Harris, J. Chem. Phys., 56(11), 5652 (1972).

41. R.A. Pearce, I.W. Levin, and W.C. Harris, J. Chem. Phys., 59(3), 1209 (1973).

42. N.C. Craig, M.N. Ackermann, and R.A. MacPhail, J. Chem. Phys., 68(1), 236 (1978).

43. E. Evans and D.L. Mills, Phys. Rev. B, 5(10), 4126 (1972).

44. C.H. Li, S.Y. Tong, D.L. Mills, Phys. Rev. B, 21(6), 3057 (1980).

45. A.L. Balch and D. Petridis, Inorg. Chem., 8(11), 2247 (1969).

46. M.N. Ackermann, R.M. Willett, M.H. Englert, C.R. Barton, and D.B. Shewitz, J. Organomet. Chem., 175, 205 (1979).

47. R.G. Little and R.J. Doedens, Inorg. Chem., 11(6), 1392 (1972).

48. R.J. Doedens, Inorg. Chem., 9(3), 429 (1970).

49. I.D. Brown and J.D. Dunitz, Acta Cryst., 13, 28 (1960).

50. N.R. Avery, W.H. Weinberg, A.B. Anton, and B.H. Toby, Phys. Rev. Lett., 51(8), 682 (1983).

51. B. Sexton, N.R. Avery, and Turney, Surf. Sci., 124, 162 (1983).

52. J.E. Demuth, H. Ibach, and S. Lewald, Phys. Rev. Lett., 40, 1044 (1978).

53. J.E. Demuth and D.E. Eastman, Phys. Rev. Lett., 32, 1132 (1974).

54. T.E. Fischer, S.R. Kelemen, and H.P. Bonzel, Surf. Sci., 64, 157 (1977).

55. M.N. Ackermann, N.C. Craig, R.R. Isberg, D.M. Lauter, and E.P. Tacy, J. Phys. Chem., 83(9), 1190 (1979).

56. Shimanouchi, T. Tables of Molecular Vibrational Frequencies, Vol. 1, 41 (National Bureau of Standards, U.S. Department of Commerce, Washington, D.C., 1972).

57. M.N. Ackermann, Inorg. Chem., 10(2), 272 (1971).

58. J.W. Nibler and V.E. Bondybey, J. Chem. Phys., 60(4), 1307 (1974).

Table 1

Vibrational frequencies ($cm^{-1}$) of $CH_3N_2CH_3$ in the gas and solid phases: a) IR gas[40] b) IR gas[42] c) IR solid[40] d) IR solid[41] e) Raman gas[42] f) Raman solid[41] g) Raman solid[40].

| Mode | | a | b | c | d* | e | f | g |
|---|---|---|---|---|---|---|---|---|
| | $a_g$ | | | | | | | |
| $\nu_1$ | $CH_3$ asym. stretch | | | | | 2989 | 2966 | 2966 |
| $\nu_2$ | $CH_3$ sym. stretch | | | | | 2926 | 2915 | 2917 |
| $\nu_3$ | N=N stretch | | | | | 1583 | 1575 | 1574 |
| $\nu_4$ | $CH_3$ asym. def. | | | | | 1437 | 1439 | 1432 |
| $\nu_5$ | $CH_3$ sym. def. | | | | | 1381 | 1386 | 1382 |
| $\nu_6$ | CN sym. stretch | | | | | 1179 | 1186 | - |
| $\nu_7$ | $CH_3$ rock | | | | | 919 | 922 | 916 |
| $\nu_8$ | CNN bend | | | | | 591 | 590 | 584 |
| | $b_g$ | | | | | | | |
| $\nu_9$ | $CH_3$ asym. stretch | | | | | - | 2977 | 2982 |
| $\nu_{10}$ | $CH_3$ asym. def. | | | | | 1440 | 1416 | 1447 |
| $\nu_{11}$ | $CH_3$ rock | | | | | 1040 | 1027 | 1026 |
| $\nu_{12}$ | $CH_3$ asym. torsion | | | | | - | 214 | 223 |
| | $a_u$ | | | | | | | |
| $\nu_{13}$ | $CH_3$ asym. stretch | - | 2981 | 2966 | 2966 | | | |
| $\nu_{14}$ | $CH_3$ asym. def. | 1438 | 1440 | 1433 | 1433 | | | |
| $\nu_{15}$ | $CH_3$ rock | 1109 | 1111 | 1112 | 1112 | | | |
| $\nu_{16}$ | CNN bend, N=N torsion | 285 | - | 312 | 312 | | | |
| $\nu_{17}$ | $CH_3$ sym. torsion | 268 | - | 222 | 222 | | | |

Table 1 (cont.)

Vibrational frequencies ($cm^{-1}$) of $CH_3N_2CH_3$ in the gas and solid phases: a) IR gas[40] b) IR gas[42] c) IR solid[40] d) IR solid[41] e) Raman gas[42] f) Raman solid[41] g) Raman solid[40].

| Mode | | a | b | c | d* | e | f | g |
|---|---|---|---|---|---|---|---|---|
| | $b_u$ | | | | | | | |
| $\nu_{18}$ | $CH_3$ asym. stretch | 2982 | 2988 | 2975 | 2975 | | | |
| $\nu_{19}$ | $CH_3$ sym. stretch | 2926 | 2925 | 2911 | 2911 | | | |
| $\nu_{20}$ | $CH_3$ asym. def. | 1445 | 1447 | 1450 | 1450 | | | |
| $\nu_{21}$ | $CH_3$ sym. def. | 1393 | - | 1386 | 1386 | | | |
| $\nu_{22}$ | CN asym. stretch | 1300 | 1112** | 1330 | 1001 | | | |
| $\nu_{23}$ | $CH_3$ rock | 1007 | 1007 | 1001 | - | | | |
| $\nu_{24}$ | CNN bend | 352 | 353 | 362 | 362 | | | |

* Reassignment of data presented in ref. 40.

** Calculated value.

Table 2

Summary of the assignments for the loss peaks observed in the $CH_3N_2CH_3$-Ni(100) spectra maintained at 300 K. Frequency values represent average values of more than a dozen spectra.

| Frequency ($cm^{-1}$) | Assignment |
|---|---|
| 328 | C-Ni stretch |
| 530 | CNN bend (perturbed), N-Ni stretch |
| 795 | H-Ni stretch; $CH_3$ rock, CH bend of $CH_2$ or $CH_3$ surface species (less likely) |
| 1012 | CNN bend, CN asym. stretch, or $CH_3$ rock |
| 1066 | $CH_3$ rock (strong impact contribution) |
| 1152 | CN sym. stretch |
| 1408 | $CH_3$ def. (strong impact contribution) |
| 1640 | N=N stretch (perturbed) |
| 2775 | $CH_3$ stretch (perturbed) |
| 2912 | $CH_3$ sym. stretch |
| 2985 | $CH_3$ asym. stretch |

Table 3

N=N stretching frequencies of selected organometallic complexes containing azo functional groups.

| Complex | N=N stretch ($cm^{-1}$) |
|---|---|
| $(t\text{-}CH_3N_2CH_3)_2PdCl_2$ | 1597[a] |
| $(t\text{-}CH_3N_2CH_3)PdBr_2$ | 1599[a] |
| $(t\text{-}CH_3N_2CH_3)PdCl_2$ | 1602[a] |
| $(t\text{-}CH_3N_2CH_3)Cu_2Cl_2$ | 1530[a] |
| $W(CO)_5(t\text{-}CH_3N_2CH_3)$ | 1531[b] |
| $[W(CO)_5]_2(t\text{-}CH_3N_2CH_3)$ | 1520[b,c] |
| $W(CO)_5(c\text{-}CH_3N_2CH_3)$ | 1522[b,d] |
| $[Cr(CO)_5]_2N_2H_2$ | 1415[e,f] |
| $[Cr(CO)_5]_2N_2D_2$ | 1415[e,f] |
| $(CH_3N_2H)CuCl$ | 1520[g] |
| $Cr(CO)_5$(t-DIPD) | 1535[h] |
| $W(CO)_5$(t-DIPD) | 1529[h] |
| $Cr(CO)_5$(c-DIPD) | 1504[h] |
| $Mo(CO)_5$(c-DIPD) | 1517[h] |
| $W(CO)_5$(c-DIPD) | 1500[h] |

a) Ref. 45. b) Ref. 23. c) Calculated value. d) N=N stretch for $c\text{-}CH_3N_2CH_3$ is 1561 $cm^{-1}$, from ref. 55. e) Ref. 28. f) N=N stretch for t-HNNH is 1529 $cm^{-1}$ and for t-DNND 1539 $cm^{-1}$, from ref. 58. g) Ref. 57. h) Ref. 46. i) N=N stretch for t-diisopropyldiazene is 1565 $cm^{-1}$ and for c-diisopropyldiazene 1560 $cm^{-1}$, from ref. 46.

Comput. 18: 326-334.

Marsh, J.L., Armstrong, T.J., Jacobson, A.P., and Smith, R.G. (1982): Health effect of occupational exposure to steady magnetic fields. Am. Indust. Hyg. Assoc. J. 43: 387-394.

Pavlicek, W., Geisinger, M., Castle, L., Borkowski, G.P., Meaney, T.F., Bream, B.L. and Gallagher, J.H. (1983): The effects of nuclear magnetic resonance on patients with cardiac pacemakers. Radiology 147: 149-153.

Vyalov, A.M. (1974): Clinico-hygienic and experimental data on the effects of magnetic fields under industrial conditions. In Kholodov, Yu. A. (ed.): "Influence of Magnetic Fields on Biological Objects." Springfield, Virginia: National Technical Information Service Report No. JPRS 63038, pp. 163-174.

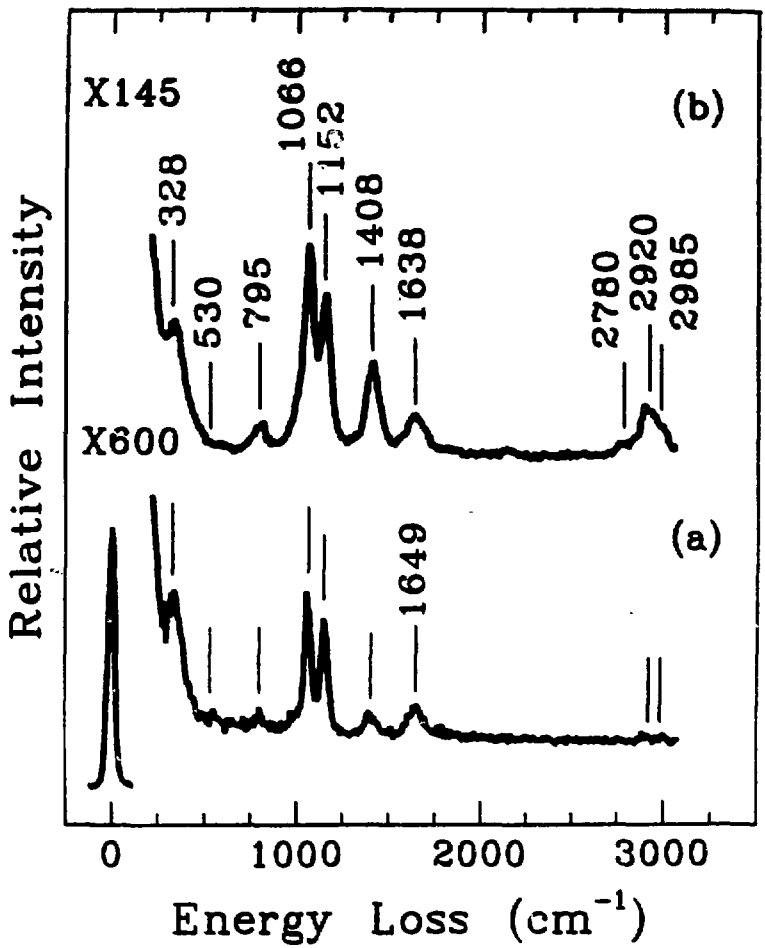


XBL 856-2723

Figure 1

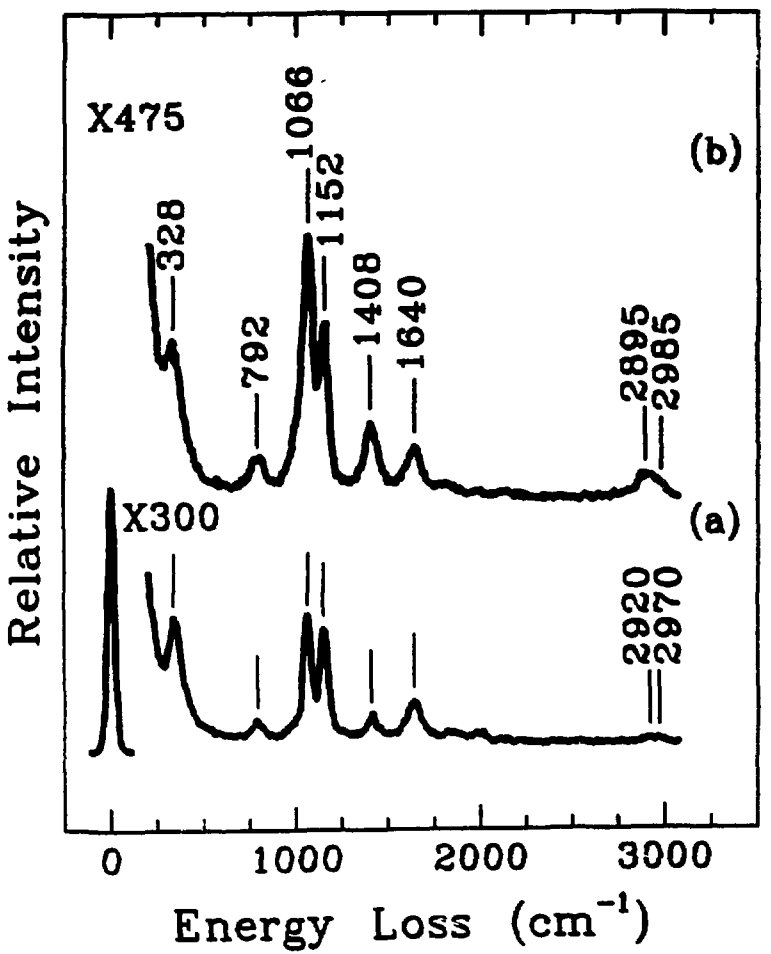


XBL 856-2724

Figure 2

$CH_3N_2CH_3$: Ni(100), ANNEALED

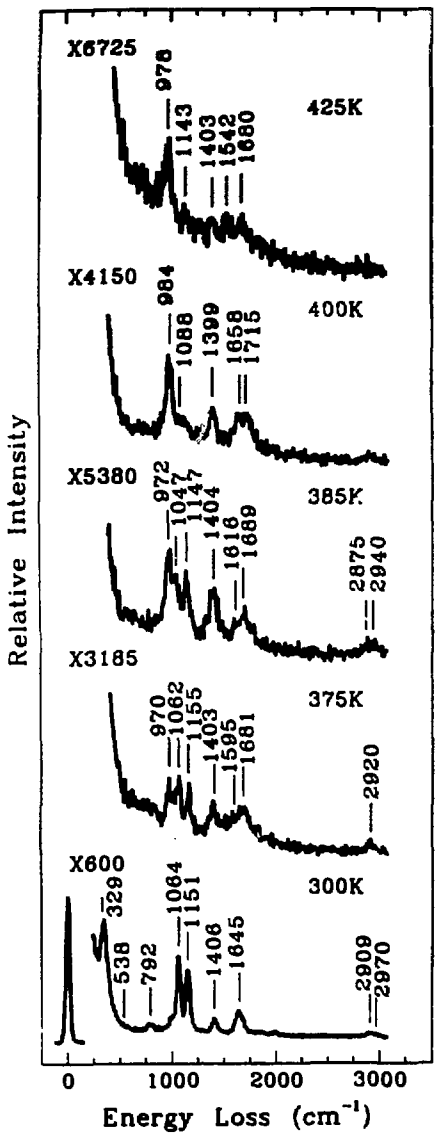


XBL 856-2729

Figure 3

# $CH_3N_2CH_3$: Ni(100), Ni(111)

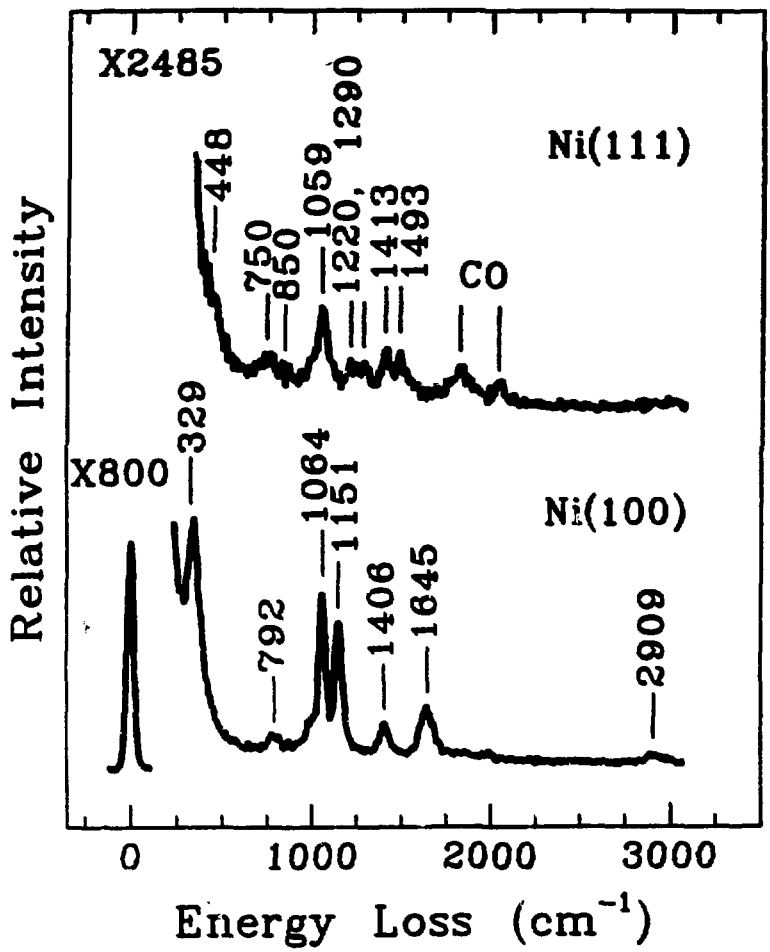


XBL 856-2727

Figure 4

# $CH_3N_2CH_3$: Cr(100)

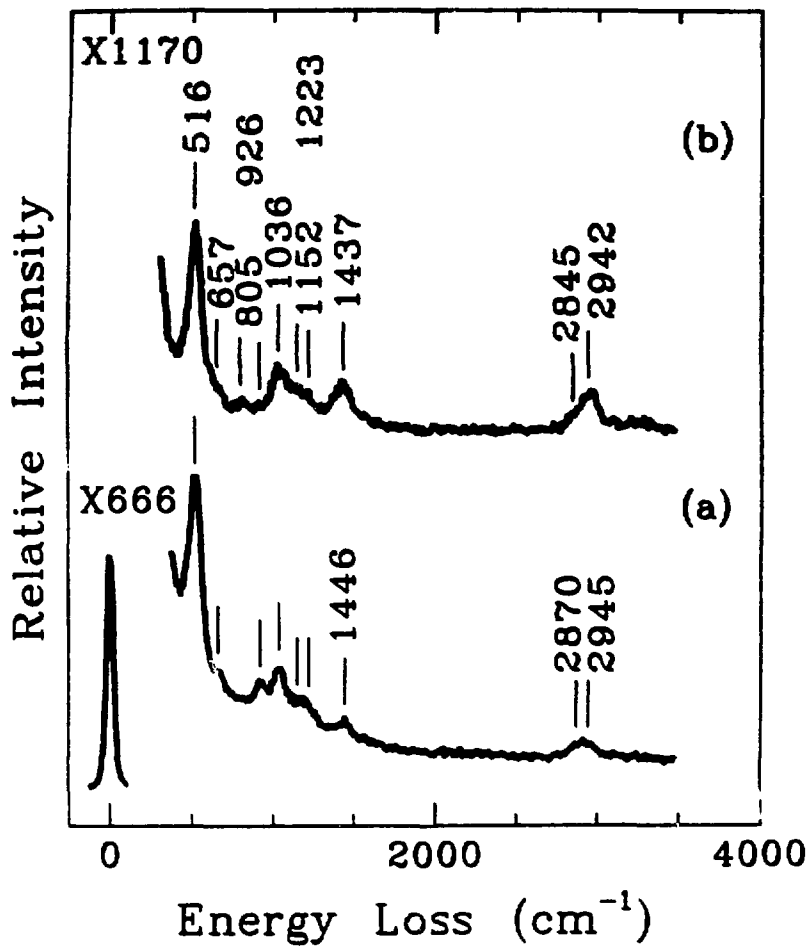


XBL 856-2726

Figure 5

# $CH_3N_2CH_3$: Cr(100), Cr(111)

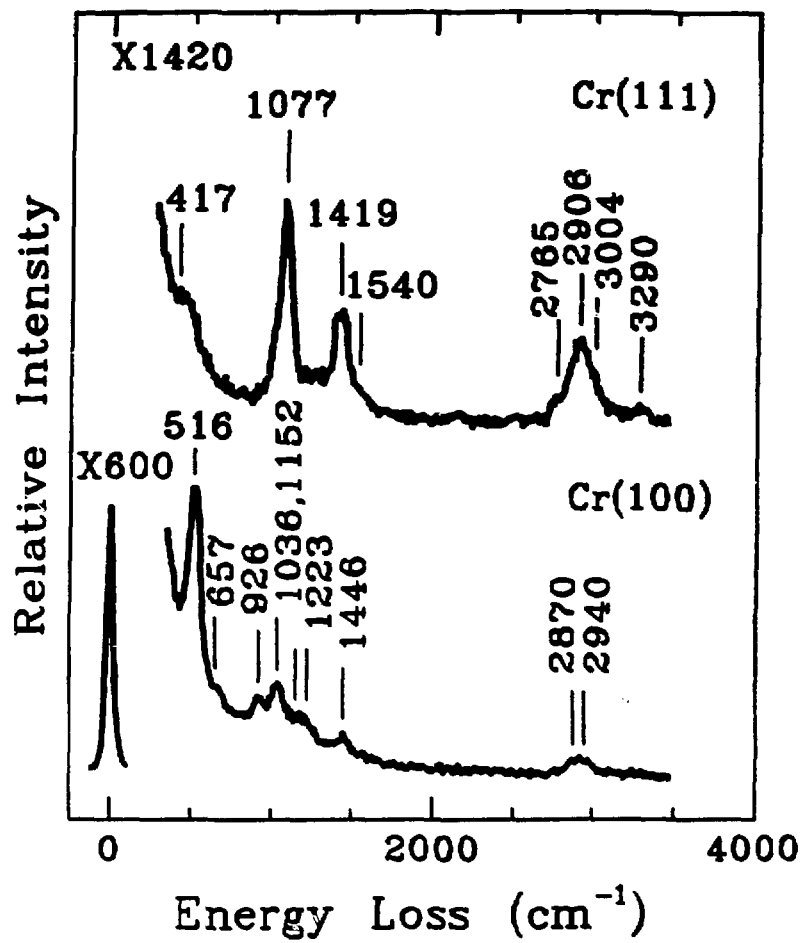


XBL 856-2728

Figure 6

## III. VARIABLE PASS MONOCHROMATOR ASSEMBLY

### A. The basic EEL spectrometer

An electron energy energy loss spectrometer has two functions; it delivers a highly monochromatic electron beam, of variable energy, to the sample, and it collects and energy analyzes the electrons which scatter off the sample. Any energy loss spectrometer consists of an electron source, a monochromator and associated optics, an interaction region, more optics, an electron energy analyzer, and, finally, an electron detector (Fig. 1). A high-stability, low-noise power supply provides potentials for the apertures, lens elements, monochromator, and analyzer. Data-acquisition is usually computer-controlled by an on-line microcomputer.

Tungsten hairpin filaments seem to be the preferred electron source among EEL spectroscopists, although other kinds of filaments, $LaB_6$ for example, may be used. For low energy systems, the monochromator, as well as the electron energy analyzer, is an electrostatic deflector which disperses the electrons as a function of their kinetic energy. An electrostatic deflector is essentially a capacitor; it consists of two parallel conductors held at different potentials. The energy of the electrons that follow a given path in the deflector gap depends on the potential difference across the gap. The focusing properties of the deflector are determined by its shape.

The 127° cylindrical deflector analyzer (CDA) and the 180° spherical deflector analyzer (SDA) are used most commonly in EEL experiments. In the spherical deflector analyzer, electron dispersion

occurs across the gap between two concentric spheres. Electrons within the desired energy range pass through a window or slit in the exit plane of the deflector. The mean energy of the electrons which are transmitted through the exit slit is known as the pass energy, $E_0$, of the analyzer. The cylindrical deflector analyzer consists of two coaxial cylinders; dispersion may occur in either the radial or the axial direction. CDAs used in EEL experiments are usually of the radially dispersing type. As with the SDA, a slit in the exit plane of the CDA selects out electrons with the desired energy. The CDA exhibits internal focusing in one dimension; the SDA in two.

The analyzer is usually the same kind of deflector as the monochromator, mainly for mechanical convenience, but also because the resolution of the analyzer should be comparable to that of the monochromator. Even though the monochromator and the analyzer may be similar physically, there are important operational differences between them. The monochromator, for example, operates under static conditions. That is, its components operate with a fixed set of voltages during any given experiment to produce a monoenergetic electron beam. On the other hand, the analyzer components are swept through a range of voltages to generate an EEL spectrum. The monochromator receives a high input current (~3 μA) with a broad energy distribution, while the analyzer receives a more monochromatic but much less intense beam (1 pA or less).

The optics associated with the source, the monochromator, and the analyzer collimate and focus the beam. Electron lenses may also

accelerate or decelerate the beam, either before or after it passes through the energy selector. Thus, the kinetic energy of the electrons incident on the sample may be different from the pass energy of the monochromator or analyzer. During the tune-up procedure, spectrometer voltages are adjusted to maximize the transmitted current and minimize the energy spread of the beam at a given pass energy. The coulomb interaction between individual electrons, as well as other non-ideal effects, limits the attainable resolution of the electron beam, so an energy spread, $\Delta E$, is always associated with the electrons which successfully traverse the monochromator exit slit. Finally, electron detection may be performed in either a single-channel or multi-channel mode.

The two beam energies of interest to an EEL spectroscopist are the pass energy and the impact energy. Again, the pass energy is the mean kinetic energy of the electrons which are transmitted through an energy selector (either the monochromator or the analyzer). The impact energy, I.E., is the energy with which electrons hit the sample; it depends only on the difference in potential between the filament (source) and the sample:

$$\text{Impact Energy} = e(\text{sample potential} - \text{filament potential}).$$

The thermal energy the electrons possess at the filament is neglected. In any monochromator, the beam energy is changed a number of times between the filament and the sample by the electron optics,

but these changes are not reflected in the impact energy.

B. Double pass monochromator assembly

The spectrometer used in this laboratory was constructed by Daniel Rosenblatt and Albert Baca between 1978 and 1982.[1] It consists of an electron gun, a two-stage monochromator (with optics), and a single-stage analyzer (with optics), and it utilizes single channel detection. Both stages of the monochromator, as well as the analyzer, are 180° spherical deflectors. The double pass monochromator assembly is shown in Fig. 2. In Fig. 2, as well as on the EEL power supply, the first stage of the monochromator assembly is referred to as the premonochromator and the second stage as the monochromator. When both deflectors are used, the spectrometer is said to be operating in a double pass mode. Configurations of the monochromator assembly using only one deflector are designated single pass.

The electron source is a hot tungsten filament (T = 2800 K). An electron beam generated by any thermionic emitter has an energetic halfwidth $\Delta E = (2.54T/11{,}600)$ eV.[2] Thus, the electron beam has an initial halfwidth of about 0.6 eV. The beam is collimated by a spherical repeller and then accelerated to the pass energy of the premonochromator and focused onto its entrance aperture by the input or A lens. The repeller helps maximize forward emission from the filament. The A lens is a 3-element aperture lens; each element is split to provide horizontal or vertical deflection. Finally, the

premonochromator aperture limits the angle, $\alpha$, at which electrons may enter the premonochromator, and it helps reduce the number of scattered electrons. The potential of the aperture is set at approximately the pass energy of the premonochromator.

The exit slit of the premonochromator serves as the entrance slit of the monochromator. The use of a two-stage energy selector significantly reduces the background on the loss side of the elastic peak. This background results from electrons which scatter off a hemisphere surface or a lens element but still pass through one sector. The chance that a scattered electron will pass through a second sector is low. The premonochromator also reduces the halfwidth of the electron beam below 0.6 eV before it enters the monochromator. The relationship between the pass energy of a 180° SDA and the hemisphere potentials is given in Appendix A.

After it passes through the monochromator exit slit, the electron beam is focused onto the sample by the zoom or B lens. This lens, another 3-element aperture lens, may act as a symmetric or asymmetric lens depending on the relationship between the pass energy of the monochromator and the impact energy. If the pass energy is greater (less) than the impact energy, the zoom lens will decelerate (acelerate) the electron beam. If the pass energy happens to equal the impact energy, the zoom lens will function as a symmetric or einzel lens. That is, the lens will focus the beam onto the sample, but it will not change the energy of the beam. The last element of the zoom lens, the sample plate, and the cover of the analyzer input

lens (the C lens) are all at ground potential, ensuring that the interaction region is field-free. The first two elements of the B lens are split for deflection as are two of the C lens elements.

The analyzer C lens is similar to the zoom or B lens. It focuses the electrons into the analyzer after they scatter off the crystal, and it changes the energy of the beam if the pass energy of the analyzer is different from the impact energy. The analyzer consists of a single 180° SDA, with a larger mean radius than that of the hemispheres used in the monochromator. The angular acceptance of the analyzer is physically limited to $\alpha = 7°$. The pencil angle of the beam at the analyzer entrance slit is usually less than this, at operating impact energies, as a result of the Abbe-Helmholtz sine law of electron optics:

$$r_a (E_a)^{1/2} \sin \theta_a = r_b (E_b)^{1/2} \sin \theta_b$$

where r is a radial dimension of the beam, E is the beam energy, and $\theta$ is the pencil angle of the beam.

As discussed in Appendix A, the pass energy of a 180° SDA is related to the radius of the inner and outer hemispheres and to the potential difference, $\Delta V = V_{in} - V_{out}$, between them. The radii of the inner and outer hemispheres are 0.85" and 1.15", respectively. The potential difference, $\Delta V$, between the inner and outer hemispheres of each of the deflectors in the monochromator assembly is controlled by one knob on the EEL power supply, permitting direct control of the

pass energy in each sector. Even though the pass energy of each sector is controlled independently of the other, the double pass design requires that both the premonochromator and the monochromator be operated at the same pass energy, because there is no way to retard the beam energy between the two SDAs. The range of available pass energies is determined by the hemisphere voltages available on the EEL power supply, which was designed for low energy, vibrational studies.

The range of impact energies is also determined by the voltage ranges available on the EEL power supply. As experiments are usually performed with the sample plate at ground, the impact energy is determined by the negative potential applied to the filament. On our spectrometer, the filament potential may be adjusted from ground to -13 volts; it is also possible to bias the crystal. Most measurements are made with an impact energy of from 1 to 5 volts, wherever the elastic signal is maximized. The impact energy is called the monochromator reference on the EEL power supply since all the monochromator (and analyzer) voltages float on it.

C. Limitations on current output of EEL spectrometers

1. Transmission

In vibrational EELS, where electrons are used to probe the vibrational motions of an adsorbed species or of a crystal lattice, the requirements on the monochromaticity of the incident beam are particularly severe. Vibrational linewidths of adsorbed species may range from 1 meV to 10 meV or more. Vibrational lines may also be

closely spaced. Thus an "ideal" spectrometer would produce an electron beam with an energy spread no greater than 1 or 2 meV FWHM. Typically, however, incident beams with a FWHM of 4–8 meV are produced. The best resolution reported to date is 2.5 meV, but it is extremely difficult to sustain practical output currents at this very high resolution.[3]

Perhaps the most severe limitation on the sensitivity of EEL spectrometers is the magnitude of the monochromatized output current. The current output of a given monochromator can be limited in a number of ways, depending on its design. The transmission of apertures, lenses, and energy selectors will determine, to a great extent, the current output. The effects of thermal components of electron velocity and space charge within the beam must also be considered. Finally, non-ideal effects (i.e., lens or selector aberrations) should be minimized.

Neglecting aberrations, the energy resolution of the 180° SDA may be expressed (Appendix B) as $\Delta E/E_0 = w/2R_0$ where $\Delta E$ is the FWHM of the triangular transmission function of the sector, $E_0$ is the pass energy, $w$ = the width of the entrance and exit slits, and $R_0$ is the mean radius of the inner and outer hemispheres. From this equation, it can be seen that the need for good resolution requires operation of the monochromator at low pass energies and the use of narrow slits. Both of these conditions reduce the current output of the monochromator. In the double pass configuration, the decrease in transmission at lower pass energies is especially harmful, because the

beam is sent through two deflectors instead of just one. The transmission of the monochromator assembly may be written as the product of the transmission functions of its components: $T_{mono.\ assem.} = t_{gun} \times t_{pre} \times t_{mono} \times t_{lens}$. In practice, the transmission tends to be much better at higher pass energies, even though $\Delta E$ increass with $E_o$. For example, when the premonochromator and monochromator are both operating at 3 eV pass energy, on the order of $2 \times 10^{-9}$ amps can be measured at the crystal. When the pass energy (in both sectors) is reduced to 0.75 eV, the current measured at the crystal decreases by two orders of magnitude.

Aside from the transmission of the deflectors, apertures, and lenses, the monochromatic output curent is most strongly limited by two things: thermal components of electron velocity and space charge. In most monochromators, electrons with thermal components of velocity are removed by the collimators and apertures in front of the energy selector. Space charge, however, can occur at a variety of locations within the monochromator. The extent to which either thermal electron velocities or space charge becomes a limiting factor on the monochromatized output current depends on the specific monochromator design. Aberrations caused by lenses, collimators, and deflectors also reduce the output current. Such aberrations increase the target image in size and angle; current is lost from the aberrated edges of the beam, and $\Delta E$ is increased. This effect is not, however, as important as the current losses resulting from space charge and thermal velocities.

2. Electrons with thermal components of velocity

Electrons are emitted from the filament with a distribution in space as well as in energy. Electrons emitted too far from the central axis of the beam or with too large a transverse momentum will not reach the entrance aperture. In other words, one limitation on the intensity of the electron beam results from the thermal components of electron velocity perpendicular to the beam direction. From the Abbe-Helmholtz sine law of electron optics, it can be shown that:

$$E_k(1 - M_T^2 \sin^2 \theta_T) = eV_T M_T^2 \sin^2 \theta_T$$

where $M_T = r_T/r_k$, k refers to the cathode, T refers to the target, and $\theta_k$ is assumed to equal $\pi/2$. By limiting $\theta_T$, the angle of arrival at the target, a limit is placed on the velocity of the electrons which reach the target. Hence, the collimating optics change the energy distribution of the beam as well as the total number of electrons arriving at the aperture (Fig. 3). It is convenient to use the energy $E_C^4$ defined as:

$$E_C = eV_T M_T^2 \sin^2 \theta_T.$$

All electrons with a kinetic energy less than $E_C$ will reach the aperture, even if they are emitted perpendicular to the beam direction, but only a fraction of the electrons emitted from the filament with energy greater than $E_C$ can pass through the

collimators. In other words, the effect of increasng $E_k$ above $E_c$ is to decrease $\theta_k$. Langmuir[4] expressed the bound to the total number of electrons whose paths can reach a given point with the half angle $\theta$ as a bound to the current density:

$$j_m = j_0(1 + \phi) \sin^2 \theta$$

for systems of axial symmetry where $j_m$ = the current density at m, $j_0$ = the initial current density, and $\phi$ = the potential at point m ($= eV_m/kT$). Even though the electron beam intensity is greatly reduced as a result of collimators, the monochromatized output current of most EEL monochromators is not limited by the electron gun.

3. Space charge

In many systems, space charge places the greatest constraints on the monochromatized current output. The term refers to the repulsive coulombic interactions between electrons in dense beams. To be more specific, space charge refers to the effect on the electrons of fields produced by charge in the beam itself, as opposed to the effect of external fields. Space charge causes directional changes in electron trajectories (it changes the overall shape of the electron beam), and it changes the energies of individual electrons. For small currents and low energy electrons, the worst problem is the action of fields perpendicular to the beam direction.

In a typical EEL monochromator, space charge may be active at the electron gun, within the deflector, or at an entrance or exit slit. Space charge is probably unavoidable at the filament and at the

selector entrance in most, if not all, EEL monochromators. Usually, however, it is the space charge spreading at the monochromator entrance slit which places the greatest restriction on monochromatized current output. Hence, simply putting in a "brighter" electron source would not necessarily improve the current output of a given monochromator. The energy broadening due to space charge repulsion in front of the selector entrance can usually be neglected, as it is just a fraction of the cathode energy spread.

Space charge may also occur within the monochromating device; if it is severe enough, it will affect the resolution (Ibach and Mills considered the effects of limiting space charge within the monochromator extensively[5]). The current density is lower after energy dispersion so space charge spreading is usually not a problem at the selector exit or at the target, unless the impact energy is particularly low. Scattering off the sample reduces the current density even more, so space charge is rarely, if ever, a problem within the electron energy analyzer.

In the double pass configuration, the current is space charge limited at the monochromator entrance but not at the premonochromator entrance. The filament and A lens are not limiting the beam intensity; we observe a maximum in monochromatic current with cathode emission. In other words, the electron gun is not operating at its brightest, so the output current is not limited by the source. Space charge spreading at the premonochromator entrance does not appear to limit the monochromatized output current either. The spectrometer has

been operated without an aperture in the premonochromator entrance plane, but no significant increase in current is observed under these conditions, although the resolution is slightly worse. The decrease in resolution is attributed to the presence of scattered electrons and to the increase in $\alpha$; the beam is not as well collimated without the entrance aperture. Finally, $\Delta E$ does not change significanty as a function of cathode current, indicating that space charge is not a drastic problem within the SDAs. An increase in $\Delta E$ with input current would indicate either an increase in the angular divergence of the beam caused by space charge within the capacitor or some other effect on electron optical conditions within the capacitor. The resolution does start to degrade at very low pass energies, below 0.65 eV, but this may be due to patchy surface potentials, stray magnetic fields, inhomogeneities in the focusing fields, charging, or other non-ideal effects.

Expressions for the maximum space charge limited current which can be passed through a given volume have been derived for a few simple geometries.[6] In these expressions, it is assumed that the current is sent through the volume so that, in the absence of repulsion, all the electrons in the beam would converge to the same point. It is also assumed that all the electrons have exactly the same kinetic energy and that the beam intensity per solid angle is independent of the inclination to the axis. Of course, the maximum current of a given diode depends on its geometry, but it is always proportional to the 3/2 power of the electron kinetic energy (i.e.,

$V^{3/2}$, where V is the anode voltage) and inversely proportional to characteristic dimensions of the diode.

Kuyatt and Simpson[7] derive a transmission function for the 180° SDA with real apertures at the entrance and exit planes. Their model yields an estimate to the current output in the case where the diameter of the entrance aperture is equal to the maximum diameter of a beam which has undergone space charge spreading. Furthermore, it predicts a maximum in the monochromatized output current as a function of the deflector pass energy. Their basic argument is presented in Appendix D. For the maximum output current of a 180° SDA with real apertures at the entrance and exit planes, Kuyatt and Simpson obtain:

$$I_{max}\ (\mu A) = 350\ E_o^{-1/2}(\Delta E_{out})^3/\Delta E_{in}$$

where $E_o$ is the pass energy of the SDA and $\Delta E_{out}$ and $\Delta E_{in}$ are the halfwidths of the outgoing and incoming beams, respectively.

D. Variable pass monochromator

The goal behind the recent changes in the monochromator assembly is to increase the current output, and particularly, the current output at low pass energies, of the monochromator. During experiments, the spectrometer is operated at the lowest possible pass energies to minimize ΔE. Unfortunately, the count rate decreases with pass energy, so in most experiments the resolution is limited by the sensitivity. In the double pass configuration, count rates of 70 -

120 KHz can be attained routinely at fairly low pass energies on clean, well-ordered surfaces. After sample dosing or in off-specular measurements, however, it is not uncommon to have to use pass energies of 2 eV or more, simply to ensure an adequate count rate to obtain a spectrum. Even at these high pass energies, the decrease in count rate can be severe. If the analyzer is moved more than 5° or 10° away from the specular direction on an adsorbate-covered surface, count rates can drop to 10 KHz or less. Thus, the decrease in count rate can be quite a serious problem, especially if good statistics are desired. In most adsorption studies (specular or off-specular), the most effective way to increase the count rate is to increase the current incident on the sample. (Multi-channel detection is another approach that could be taken.)

The strategic advantage of the variable pass monochromator assembly is that it allows operation of the premonochromator at high pass energies, while the monochromator is operated at low pass energies, thereby increasing the current output without sacrificing resolution. The improvement in the current output in the variable pass configuration will arise from the increased transmission of the premonochromator at the higher pass energies at which it will operate. Both Read et al.[8] and Froitzheim[9] have suggested that by sending the beam through a premonochromator, which can be operated at high pass energies, before it experiences the more stringent energy selection of the monochromator, operating at low pass energies, one can reduce the attenuation of the beam caused by space-charge

spreading at the selector entrance. The "pre-selected" beam will, of course, have to pass through a retarding lens before it enters the monochromator. Read et al.[8] did not give any estimate of the improvement in the monochromatized output current that could be expected with this kind of arrangement. Froitzheim[9] made a crude estimate for the 127° CDA but did not fully account for the influence of the energy dispersion on the magnitude of the output current.

In the double pass configuration, the premonochromator does reduce the space charge spreading at the monochromator entrance relative to a configuration in which the electron gun sits immediately in front of the selector entrance (i.e., the single pass configuration). The current density of the beam is lower after it has gone through the premonochromator than at the filament; electrons with thermal components of velocity perpendicular to the beam direction are largely eliminated from the beam, and the beam has already undergone some energy dispersion. So the effects of space charge at the monochromator entrance slit are smaller in the double pass mode than they would be without the premonochromator (single pass mode). On the other hand, when both the premonochromator and the monochromator are operated at low pass energies, transmission losses are very high. In the variable pass configuration, a high current, low resolution beam will be extracted from the premonochromator, operating at a high pass energy, and then sent through the monochromator, at a lower pass energy, to improve its resolution.

In order to see an increase in the monochromatized output

current, the maximum current which can be transported through the monochromator entrance slit will have to increase. By operating the premonochromator at higher pass energies than the monochromator, we are increasing the current density at the monochromator entrance, relative to the double pass configuration, for any given monochromator pass energy. Operation of the hemispherical sectors at different pass energies requires the construction of a retarding lens between them. Even accounting for transmission losses in the retarding lens, there should be an increase in current density at the monochromator entrance slit in the variable pass mode. If there is an increase in the space charge spreading at the monochromator entrance slit, it will have to be more than offset by the increase in beam intensity for any improvement in the output current to be observed. The focusing ability of the D lens may also help compensate any potential cut-off of current due to space charge broadening at the monochromator entrance slit. The modifications to the monochromator assembly will not totally eliminate the space charge spreading at the monochromator entrance slit, although they should lessen its severity. The slit potential will still be low at low pass energies, and space charge spreading cannot really be avoided. It will still be a limiting factor on the current output.

The modifications basically involved the installation of a new 3-element aperture lens between the two monochromator hemispheres, permitting the premonochromator and monochromator to operate at different pass energies. The addition of the D lens changed the

distance between the exit plane of the monchromator and the sample, making it necessary to redesign the B lens. The input (A) lens is the same in both the double pass and variable pass configurations (Fig. 4).

Until the modifications were made to the EEL monochromator assembly, the upper limit to the pass energy of either selector was only slightly greater than 3 eV (restricted by the voltage ranges on the EEL power supply). The lowest pass energy used has been about 0.65 eV. On clean, well ordered surfaces, pass energies of about 0.75 eV can be used routinely. The lower limit to the pass energies is not restricted by the supply but rather by the onset of degradation in the resolution. The range on the premonochromator voltages has been extended so that pass energies up to 10 eV may be attained in the first selector. The upper limit to the pass energy in the monochromator is still 3 eV.

A very crude estimate of operating currents attainable with the variable pass design can be made, using current measurements taken with previous configurations of the monochromator. In 1981, the input lens and the zoom lens of the monochromator assembly were both different from the corresponding lenses when the variable pass design was first considered. At this time, however, experiments were performed in both the single pass and the double pass modes with the same lens conditions in each case. By comparing the current output in the two cases at the same pass energy (Table 1), it is possible to get an empirical idea of the attenuation of the beam in going from single pass to double pass operation. It is clear from Table 1 that the

single pass current is approximately 50X more than the double pass current at 1 eV pass energy. The resolution (at 1 eV) is worse by more than a factor of 3 in the single pass mode, however, 60 meV vs. 17 meV, and the background due to scattered electrons is much higher than that in the double pass mode. (The current was measured by a channeltron and corrected for gain.)

Current measurements taken at various parts of the monochromator assembly, in the double pass configuration (Table 1), can be used to make a rough estimate of the transmission of one of the 180° SDAs if it was used without an exit slit. Measurements of the current to the premonochromator exit slit cannot be used to give an indication of the premonochromator output current, because, in the double pass configuration, the premonochromator entrance and exit slits are not electrically isolated from one another, and the entrance slit is almost immediately in front of the filament. Under typical operating conditions in the double pass mode ($E_0$ = 3 eV), the premonochromator transmits an electron beam with an energy halfwidth of about 0.045 eV. The energy halfwidth of the beam at the filament is about 0.6 eV. Assuming that $j_{out} = j_{in} \cdot T \cdot (\Delta E_{out}/E_{in})$ (Appendix B), a simplistic argument, that the current has been reduced by a factor of ~13 as a result of the slit width can be made. Multiplying the observed current to the monochromator outer hemisphere, $7 \times 10^{-8}$ amps by 13 yields an estimate of the premonochromator output if the exit slit was removed: $7 \times 10^{-8}$ amps $\times$ 13 = $9.1 \times 10^{-7}$ amps. The current at the filament is about $3 \times 10^{-6}$ amps, so the transmission

of the premonochromator can be calculated: $(9.1 \times 10^{-7}/3 \times 10^{-6}) \times 100\% = T \approx 30\%$.

By using these two rough calculations, for the attenuation the beam experiences in double pass vs. single pass energy selection and for the transmission of the sectors in this spectrometer, along with current measurements to the sample made at a range of pass energies with recent lens conditions (Table 2), it is possible to make a very crude estimate of the current output which can be expected with the variable pass design. Assuming that the beam current is reduced by a factor of 50 upon passage through the monochromator (Table 1), the current output of the premonochromator at high pass energies in the double pass configuration can be "calculated." Current measurements to the monochromator outer hemisphere would also give an indication of the premonochromator output, but such measurements are not available for the most recently used lenses.

From Table 2, the current to the crystal at high pass energies (3 eV) is approximately $1.5 \times 10^{-9}$ amps. Multiplying this figure by 50 yields an estimate of the premonochromator "output". Thus, if the premonochromator is operated at 3 eV in the variable pass mode, the current incident on the retarding lens is calculated to be $7.5 \times 10^{-8}$ amps. The incident current will be even higher if the premonochromator is operated at a higher pass energy. The monochromator is operated at lower pass energies, 0.5 to 1.0 eV, and a narrow slit is placed in the monochromator exit plane, to reduce $\Delta E$ to approximately 0.006 eV. Using $j_{out} = j_{in} \cdot T \cdot (\Delta E_{out}/E_{in})$, (7.5

X $10^{-8}$)(.006/.045)(30%) = 3.7 X $10^{-9}$ amps.

In this estimate, it has been assumed that the total current leaving the premonochromator will be transmitted through the D lens, but this is not the case. Transmission losses are certainly expected; furthermore, the extent of such losses may depend on the retardation the beam experiences between the premonochromator and the monochromator. Even if the transmission through the D lens is only 10%, however, the output current will be on the order of $10^{-10}$ amps, an order of magnitude improvement over the current output available in the double pass mode.

Kesmodel[3] recently reported the operating characteristics of a spectrometer designed with similar strategy. The two-stage monochromator utilizes two 127° CDAs with an intermediate 6-element lens system to focus and collimate the beam from stage 1 to stage 2. This lens system consists of a 3-element asymmetric lens, a 2-element out-of-plane focusing lens, and a collimation slit. Kesmodel obtained current to the sample of 1.3 X $10^{-10}$ amps, with a monochromator pass energy of 1.0 eV and an overall system resolution of 3.2 meV. He has indicated that beam currents as high as 2 X $10^{-8}$ amps can be measured at the sample, with an energy resolution in the 6-9 meV range, by operating the premonochromator at 4 eV pass energy and the monochromator at 2 eV pass energy.[10] Thus, it may not be necessary, in the variable pass configuration, to operate the monochromator at very low pass energies to maintain acceptable resolution, and it seems reasonable for us to expect currents to the crystal on the order of

$10^{-10}$ amps under conditions of low pass energy and high resolution.

The D lens and the new B lens were designed using focal length data from Harting and Read.[11] Both are 3-element aperture zoom lenses. For a fixed object position and object energy and a fixed image position, both lenses require that the image energy be variable. Hence, each lens must provide two variable voltage ratios. A minimum of three lens elements is required to provide two variable voltage ratios: $V_1/V_3$ is used to change the potential of the image point and $V_2/V_3$ is used to control the focusing strength of the lens. For the D lens, physical constraints limited the total focal length (object + image distance) from about 0.4" to about 0.75"; a focal length of 0.600" was chosen. The focal length of the B lens is increased by almost the same amount to accomodate the presence of the D lens (Fig. 4).

The D lens is a 3-element aperture lens; each element is split to provide horizontal or vertical deflection. Theoretically, the potential of the first lens element, D1, should correspond to the pass energy of the premonochromator and that of the third element, D3, to the pass energy of the monochromator. $V_1/V_3$ can therefore range from about 10 to 1.2, depending on the pass energy in each sector, although most of the time the spectrometer will probably be operated at the low end of the voltage ratio. $V_2/V_3$, obtainable from the Harting and Read data, is a function of $V_1/V_3$, but it also depends on the relative object and image distances as well as on the magnification factor. Harting and Read present the data in their lens

calculations in terms of a fundamental unit of length. For 3-element aperture lenses, the aperture diameter, D, is taken as this fundamental unit of length. Following Harting and Read's notation, the final lens dimensions are as follows: D (aperture diameter) = 0.100", A (spacing between lens elements) = 0.050", P (object distance) and Q (image distance) = 0.300". The lens elements were machined from 0.010" thick molybdenum. The desired magnification of the D lens is -1; the actual magnification ranges from about -0.6 to -1.2, depending on the retardation.

The distance between the exit plane of the monochromator and the sample is 2.24" in the double pass configuration; in the variable pass configuration, it is increased to 2.79" to provide sufficient space for mounting the D lens. Since this distance corresponds to the focal length of the B lens, changing it meant that the B lens had to be redesigned to maintain a good focus on the sample. In the new B lens, the existing apertures were used (D = 0.310", A = .150"); that is, only the relative object and image distances were changed. The ratio of the object distance to the image distance is now 2:7.

The potential of the first B lens element should correspond to the pass energy of the monochromator, while the potential of the third element should correspond to the negative of the impact energy. The B lens may either accelerate or retard the electron beam, depending on the relationship between the monochromator pass energy and the impact energy. Again, the voltage of the second element depends on the ratio $V_1/V_3$ and is obtainable from the Harting and Read data. In order

to maintain the full dynamic range of the impact energy (0-13 eV), the B lens was originally redesigned to operate with a magnification of -2 to -3. In the usual range of impact energies used in this laboratory, however, (1-5 eV), a magnification of -1 is more desirable. Redesigning the B lens with new lens elements (i.e., new values of D) would be relatively easy to do, and it would allow the B lens to operate with a magnification of -1.

The modifications required a new mounting plate, which could accomadate both sets of hemispheres and the D lens, and 9 new voltages at the chamber. Six of the voltages are for the D lens elements; the other three are for the entrance and exit slits; all must float on the impact energy. One of the advantages of the variable pass configuration is that all the deflector entrance and exit slits are electrically isolated from one another. In the double pass configuration, the premonochromator entrance aperture and exit slit, as well as the monochromator exit slit, were all at the same potential. In the new arrangement, the potential of each slit can be set independently of the others, and the current can be measured to any one independently of the others.

The design work and machining have been completed, as have the modifications to the power supply. The new monochromator has been assembled and is currently being characterized. The tuning procedure for the variable pass configuration is slightly different than that for the double pass configuration, because there are more places where current measurements can be made. For example, in the double pass

configuration, the current was maximized at the premonochromator entrance aperture, the premonochromator outer hemisphere, the monochromator outer hemisphere, and finally at the sample. In the new configuration, the current is maximized to the premonochromator entrance aperture, the premonochromator outer hemisphere, the premonochromator exit slit, the monochromator entrance slit, the monochromator outer hemisphere, the monochromator exit slit, and then at the sample.

It is much easier to find the beam at high pass energies and then tune down to operating pass energies than to start tuning at low pass energies. At the beginning of the tune-up, the hemisphere and lens potentials are set to reasonable initial values, and the deltas (for the A, B, and D lenses) are set to zero. The current to the premonochromator entrance aperture is maximized by adjusting the voltages (levels and deltas) on the A lens, as well as the voltage on the repeller. Once the current to the premonochromator entrance aperture is maximized, the same process is used to maximize the current to all the other components of the monochromator assembly. During each step of the tuning procedure, all previous voltages seen by the beam must be adjusted to maximize the current. Currents to the various components of the monochromator assembly are measured with a picoammeter or with a current amplifier combined with a digital voltmeter.

Once the beam has reached the monochromator exit slit, the current to the crystal is optimized using primarily the D lens, B

lens, and monochromator voltages. A true beam can be checked in two ways. (1) The beam should be very sensitive to the hemisphere voltages and should go through a sharp maximum as a function of each hemisphere voltage. (2) The beam current should also go through a sharp maximum as a function of the filament current (between 1.9 and 2.1 amps). After the beam is focused onto the sample, it is scattered into the analyzer. The crystal must be clean and well ordered, and the sample and analyzer must be at the proper angles. The current to the analyzer entrance slit is maximized using the B and C lens voltages and the analyzer reference. Finally, the beam is tuned into the detector using the analyzer hemisphere voltages and the C lens. The spiraltron should always be checked before the last step is attempted, to make sure it is working correctly. Two easy tests are turning on the ion gauge filament and the heater filament while the spiraltron high voltage is on and watching the dark count rate. It should increase from one or two counts every 10 seconds to hundreds of counts a minute.

## References


1. D.H. Rosenblatt, Ph.D. thesis, University of California, Berkeley, 1982 (LBL-14774, unpublished).
2. J.A. Simpson and C.E. Kuyatt, J. Appl. Phys., 37(10), 3805 (1966).
3. L.L. Kesmodel, J. Vac. Sci. Technol., A 1(3), 1456 (1983).
4. D. Langmuir in J.R. Pierce, Theory and Design of Electron Beams (D. Van Nostrand Company, Inc., New York, 1954).
5. H. Ibach and D.L. Mills, Electron Energy Loss Spectroscopy and Surface Vibrations (Academic Press, New York, 1982).
6. I. Langmuir and K. Blodgett, Phys. Rev., 24, 49 (1924).
7. C.E. Kuyatt and J.A. Simpson, Rev. Sci. Instr., 38(1), 103 (1967).
8. F.H. Read, J. Comer, R.E. Imhof, J.N.H. Brunt, and E. Harting, J. Electron Spectrosc. Related Ph., 4, 293 (1974).
9. H. Froitzheim, J. Electron Spectrosc. Related Ph., 34, 11 (1984).
10. L.L. Kesmodel, private communication.
11. E. Harting and F.H. Read, Electrostatic Lenses (Elsevier Scientific Publishing Company, New York, 1976).

## Table 1

Current measurements (amps) taken in the double pass and single pass configurations. The monochromator had the same input (A) lens and the same zoom (B) lens in both configurations. In the double pass configuration, the current was measured at the premonochromator outer hemisphere (P.O.H.), at the monochromator outer hemisphere (M.O.H.), and outside the monochromator assembly with a channeltron (Ichan, current was corrected for  in). In the single pass configuration, the current was measured at a channeltron outside the monochromator assembly.

| $E_o$ (eV) | Double Pass | | | Single Pass |
|---|---|---|---|---|
| | P.O.H. | M.O.H. | Ichan | Ichan |
| 4[1] | $3 \times 10^{-6}$ | $7 \times 10^{-8}$ | $1.4 \times 10^{-11}$ | |
| 2 | $2 \times 10^{-6}$ | $2 \times 10^{-8}$ | $5 \times 10^{-13}$ | |
| 1 | $1.8 \times 10^{-6}$ | $6 \times 10^{-9}$ | $4 \times 10^{-14}$ | $2 \times 10^{-12}$ |
| 0.75 | | | | $2 \times 10^{-14}$ |

1 These current measurements were made in 1981. The power supply for the EEL spectrometer in use at this time permitted operation of the monochromator and premonochromator at pass energies greater than 3 eV.

Table 2

Current measurements (amps) to the crystal taken in the double pass configuration, with the input (A) lens and the zoom (B) lens described in the Ph.D. thesis of D.H. Rosenblatt.[1] In the third column, the current has been multiplied by a factor of 50 to give an estimate of the current available if the spectrometer was operated in the single pass configuration with these lenses.

| Eo (eV) | Icrystal | X50 |
|---|---|---|
| 3 | $1.5 \times 10^{-9}$ | $7.5 \times 10^{-8}$ |
| 1 | $4 \times 10^{-11}$ | $2 \times 10^{-9}$ |
| 0.75 | $2.2 \times 10^{-11}$ | $1.1 \times 10^{-9}$ |

## Figure Captions

Figure 1. Block diagram of an energy loss spectrometer.

Figure 2. Cross-sectional illustration of the electron monochromator in the double pass configuration.

Figure 3. Representation of the effects of the collimators and energy selector on the intensity and energy distribution of the electron beam emitted by the cathode.

Figure 4. Cross-sectional illustration of the electron monochromator in the variable pass configuration.

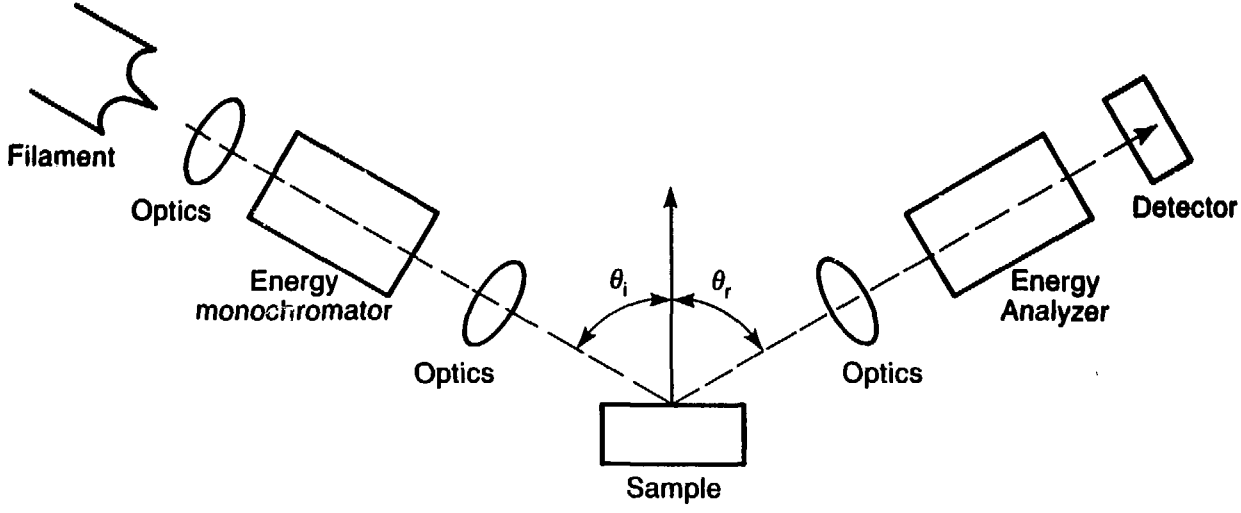


XBL 856-11191

Figure 1

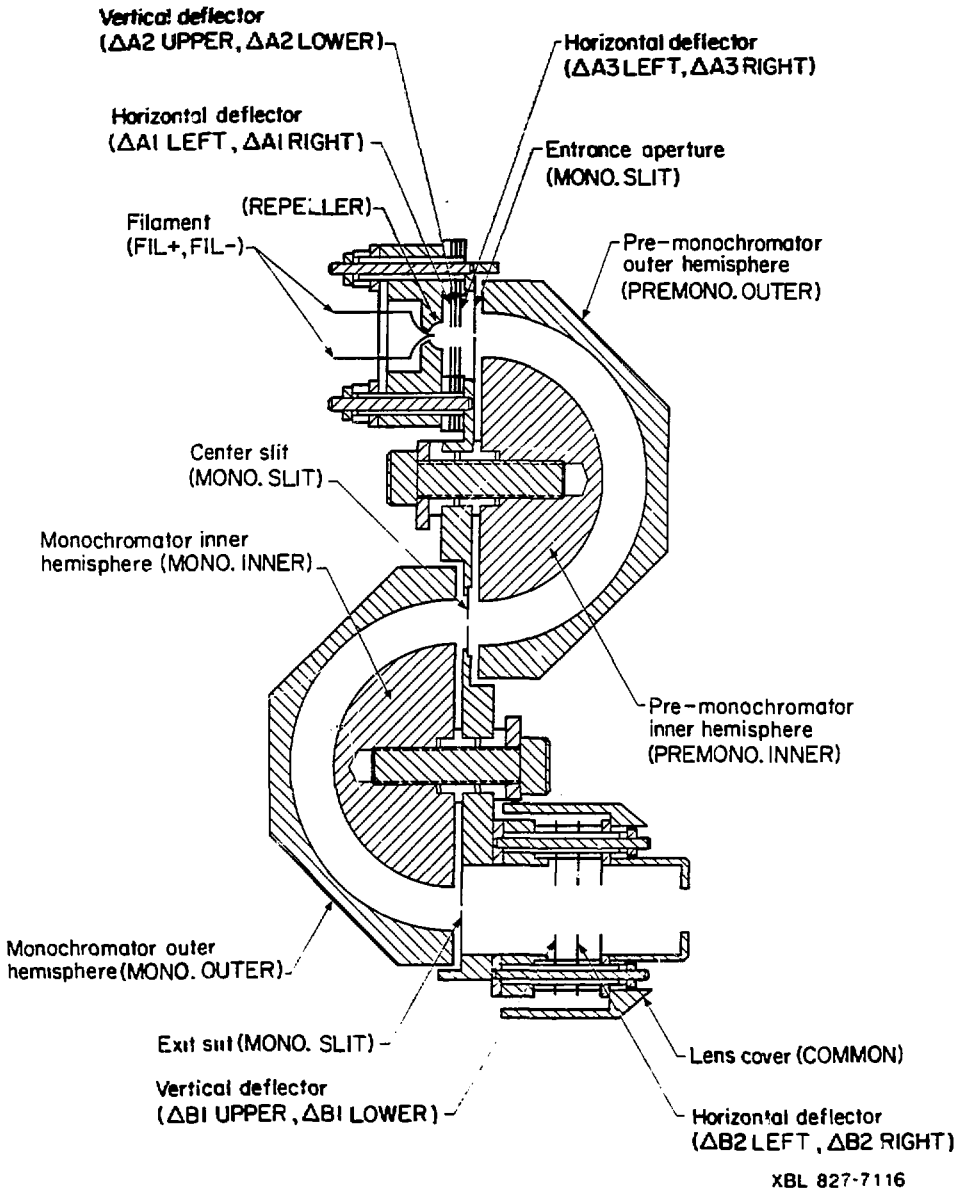
EELS ELECTRON MONOCHROMATOR
Vertical deflector
(ΔA2 UPPER, ΔA2 LOWER)
Horizontal deflector
(ΔA3 LEFT, ΔA3 RIGHT)
Horizontal deflector
(ΔA1 LEFT, ΔA1 RIGHT)
Entrance aperture
(MONO. SLIT)
(REPELLER)
Filament
(FIL+, FIL-)
Pre-monochromator
outer hemisphere
(PREMONO. OUTER)
Center slit
(MONO. SLIT)
Monochromator inner
hemisphere (MONO. INNER)
Pre-monochromator
inner hemisphere
(PREMONO. INNER)
Monochromator outer
hemisphere (MONO. OUTER)
Exit slit (MONO. SLIT)
Lens cover (COMMON)
Vertical deflector
(ΔB1 UPPER, ΔB1 LOWER)
Horizontal deflector
(ΔB2 LEFT, ΔB2 RIGHT)
XBL 827-7116

**Figure 2**

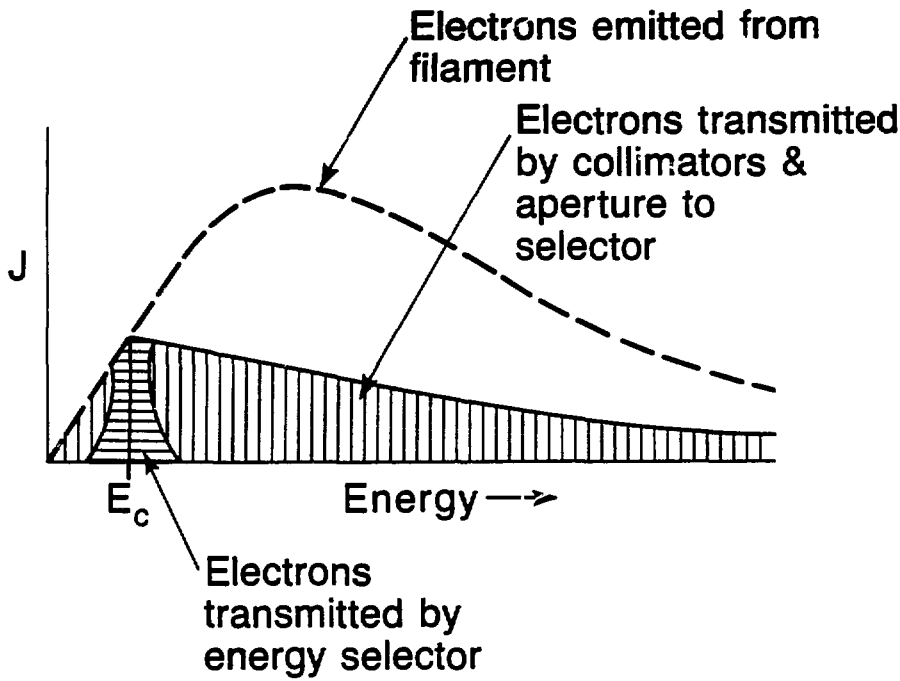


XBL 856-11192

Figure 3

EELS ELECTRON MONCHROMATOR

VARIABLE PASS

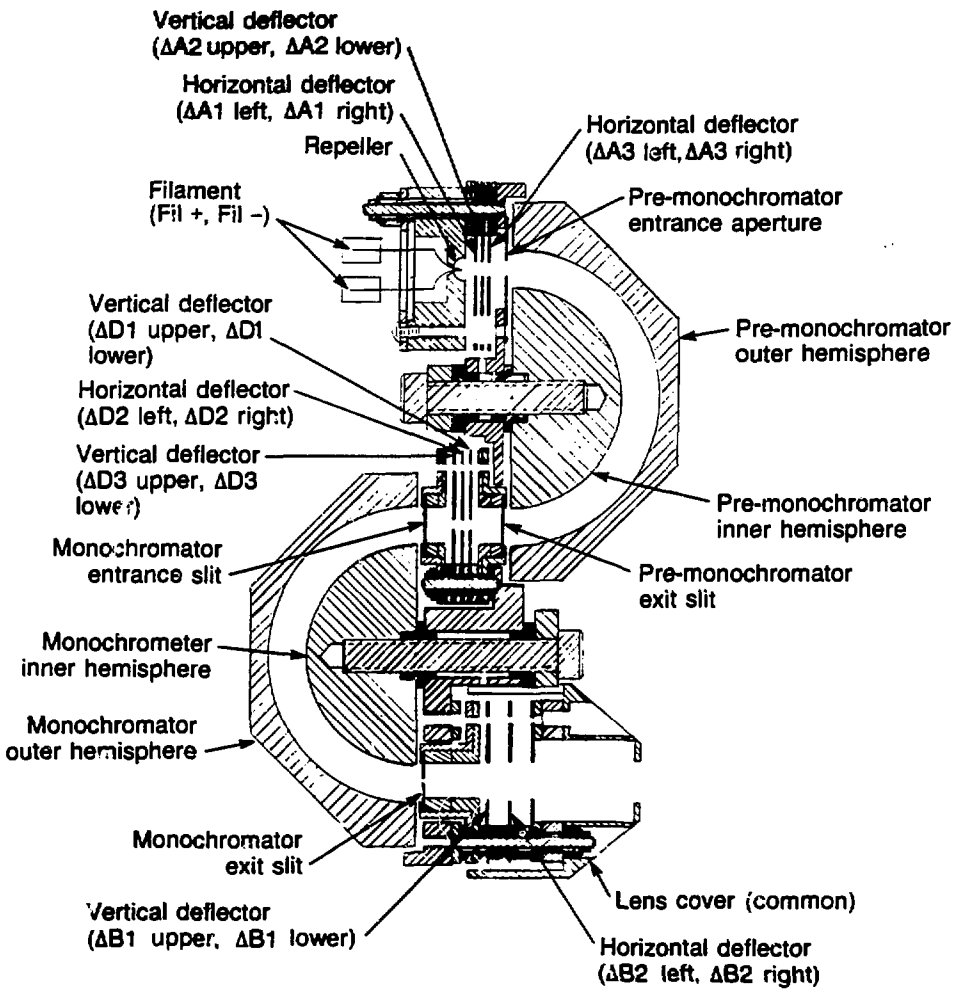


XBL 856-11194

Figure 4

## APPENDIX A

The pass energy of a 180° SDA is determined by the radius and the potential of the inner and outer hemispheres. According to Kuyatt and Simpson[1], the potential of the inner ($V_{in}$) and outer ($V_{out}$) hemispheres may be expressed by:

$$V_{in} = [2(R_o/R_{in}) - 1]\, E_o \text{ and } V_{out} = [2(R_o/R_{out}) - 1]\, E_o \quad (1)$$

where $E_o$ is the pass energy and $R_o$ is the mean radius of the inner ($R_{in}$) and outer ($R_{out}$) hemispheres. The radial electric field in the gap between the inner and outer hemispheres of the deflector is determined by $\Delta V$ ($= V_{in} - V_{out}$), the potential difference between the inner and outer hemispheres, and by the radii of the two hemispheres. It has an $r^{-2}$ dependence.

$$\vec{\epsilon}(\vec{r}) = \frac{\Delta V\, R_{in} R_{out}}{(R_{out} - R_{in})\vec{r}^2} \quad (2)$$

An electron with mass M and velocity $\vec{v}$ in the deflecting field will travel along the center path of radius $R_o$ if the centripetal force it experiences is balanced by the force of the deflecting field along that path.

$$\frac{M\vec{v}^2}{R_o} = e\epsilon(R_o) = \frac{e\Delta V\, R_{in} R_{out}}{(R_{out} - R_{in})R_c^2} \quad (3)$$

$$\frac{M\vec{v}^2}{2} = E_o = \frac{e\Delta V\, R_{in}R_{out}}{2(R_{out}-R_{in})R_o} \qquad (4)$$

Those electrons with energy satisfying relation (4) will be focused onto the slit at the exit plane of the sector. The potentials of the entrance slit and exit slit are usually set at the pass energy of the deflector.

## References

1. C.E. Kuyatt and J.A. Simpson, Rev. Sci. Instr., 38(1), 103 (1967).

## APPENDIX B

Assuming the energy distribution of the input current is constant within the range of the energy basewidth of the exit current, the output current density, $j_{out}$ of a given monochromator can be described by the expression:

$$j_{out} = j_{in} \cdot T(E,\alpha,w,\text{geometry}) \cdot (\Delta E_{out}/\Delta E_{in})$$

where $j_{in}$ is the input current density, $\Delta E_{in}$ and $\Delta E_{out}$ are the halfwidths of the incoming and outgoing beams, and T is a function describing the transmission of the monochromating device. The transmission function is essentially a figure of merit used to describe the performance of a given device; it can be defined in a number of ways. Ideally, it will describe the transmission as a function of energy, taking account of the electron distribution over space and angle, but approximate transmission functions can be very useful.

A simple transmission function for the 180° SDA can be derived from the equation for the electron trajectories[1]: (Fig. 1)

$$x_2 = -x_1 + 2R_0\Delta E/E_0 - 2R_0\alpha^2$$

where $x_1$ ($x_2$) is the radial distance of an incident (out-going) electron measured from the path of radius $R_0$. Consider the case where the entrance and exit slits are the same width. Set $x_1 = x_2$

$= 1/2(w)$ and neglect $\alpha^2$:

$$w = 2R_0\Delta E/E_0 \qquad \text{or} \qquad \Delta E/E_0 = w/(2R_0).$$

The last equation shows clearly the relationship between resolution, $\Delta E$, slit width, $w$, pass energy, $E_0$, and deflector size, $R_0$. To minimize $\Delta E$, it is necessary to maximize $R_0$ and minimize the slit width and the pass energy. The transmission function may be defined as the fraction of the entrance slit which is imaged on the exit slit:

$$T = w_{exit}/w_{entr}$$

From the equation for the electron trajectories, one can see that the entrance slit is imaged with a magnification of -1, but that it is shifted (in the radial direction) by an amount $2R_0\Delta E/E_0$. Thus, (neglecting $\alpha$)

$$T = (w_{entr} - 2R_0\Delta E/E_0)/w_{entr} = 1 - (2R_0/w)\Delta E/E_0$$

and the transmission is a triangular function of $\Delta E/E_0$.

## References

1. C.E. Kuyatt and J.A. Simpson, Rev. Sci. Instr. 38(1), 103 (1967).

## Figure Captions

Figure 1. Cross section of a 180° spherical deflector analyzer.

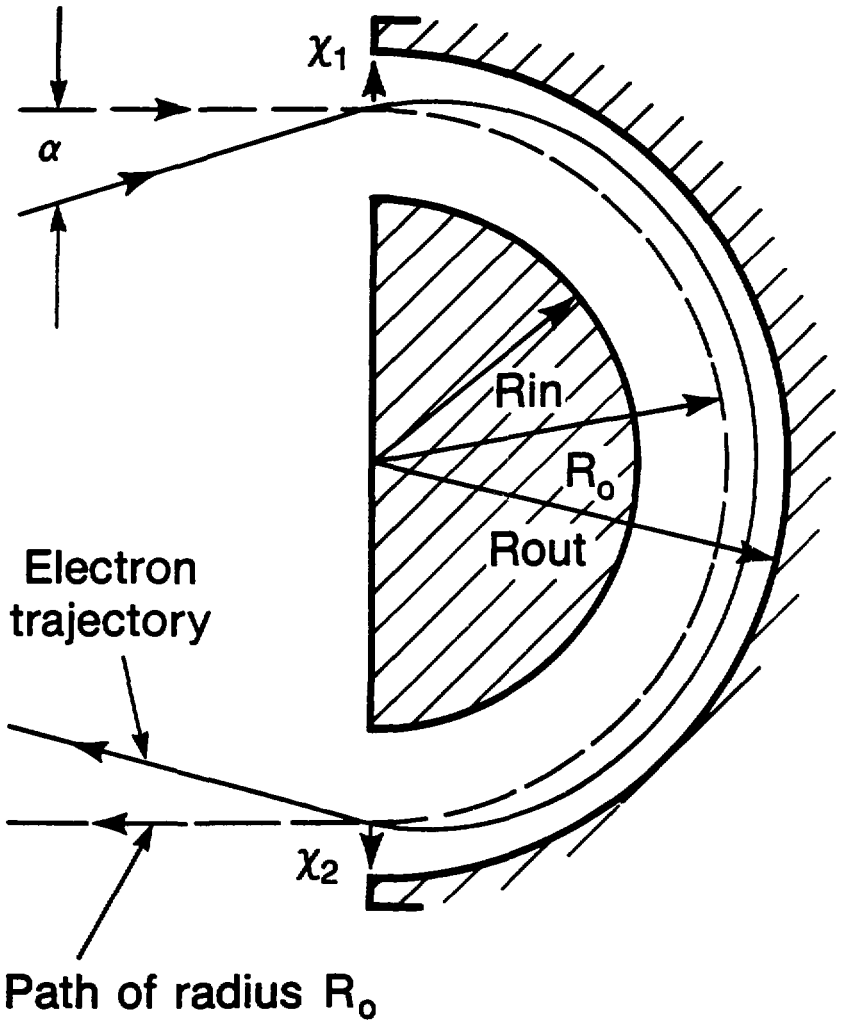


XBL 856-11190

Figure 1

## Appendix C

In their model, Kuyatt and Simpson[1] use the expression for the maximum current (in μA) which can be forced through a tube of a given length, L, and diameter, D:

$$I_{max}\ (\mu A) \quad = \quad 38.5\ V^{3/2}\ (D/L)^2 \quad = \quad 38.5\ V^{3/2}\ \alpha^2$$

where V is the anode voltage corresponding to the pass energy of the tube.[2]

The space charge equation for electron flow between concentric spheres has been solved but is not an appropriate model when the spheres are being used to energy analyze an electron beam rather than as an emitter-collector pair.[3] The tube model is closer, especially if the internal focusing of the SDA can be mimicked.

Kuyatt and Simpson model the deflector as a tube of length $\pi R_0$ and width w, and they model its focusing ability by concentrating focal properties in two thin lenses, one at $\pi R_0/4$ and one at $3\pi R_0/4$. Again, the diameter of the entrance aperture is assumed equal to the maximum diameter of the beam, so that all of the incident current may be used. The unknown in the expression for $I_{max}$ is $\alpha$ (= D/L). In the crudest model, $\alpha = w/\pi R_0$, but this value of $\alpha$ neglects the internal focusing ability of the SDA.

By taking $\alpha$ as $w/\pi R_0$, $R_0 = 1"$, and $w = 0.006"$, and using appropriate values of the slit voltage, $V_s$, calculated values of the maximum current that can be forced through one 180° SDA at various

pass energies may be obtained. At high pass energies, $V_s = 3$ V for example, $I_{max} = 7.2 \times 10^{-10}$ amps. At low pass energies, $V_s =$ 0.75 V, and $I_{max} = 9.1 \times 10^{-11}$ amps. According to this model, if the pass energy is reduced by a factor of X, the current is reduced by a factor of $X^{3/2}$. Actually, the estimate of $I_{max}$ at the higher pass energy is lower than the monochromatized output current available from the EEL spectrometer when it is operated in the double pass configuration. That is, despite the fact that the beam passes through two deflectors in the spectrometer (as well as two lenses), at high pass energies, the observed transmission is better than that predicted by this simple model. The discrepancy may arise because the model neglects the internal focusing of the 180° SDA. Furthermore, the "tube" diameter in the above estimate is taken as the slit width of 0.006", but the gap between the inner and outer hemispheres of both the premonochromator and the monochromator is 0.300". The estimate to the current output available at low pass energies, however, is higher than the observed current output of the (double pass) spectrometer. The strong reduction in current observed at low pass energies may reflect transmission losses the beam experiences as it passes through the two 180° deflectors. Such transmission losses certainly become more problematic at lower pass energies.

By using the relationship between the minimum (focused) and the maximum (space charge spread) diameter of an electron beam forced through a tube, $w_{min} = D/2.35$[1], and by modeling the focal properties of the SDA, Kuyatt and Simpson obtain $w_{min} = 2R_o\alpha/3$ or $\alpha = 3w_{min}/2R_o$.

Using this value of $\alpha$, $I_{max} = 38.5\ V^{3/2}\ (3w_{min}/2R_o)^2$. In terms of the pass energy and the resolution, $\alpha/3 = w/2R_o = \Delta E/E_o$ and $\alpha^2 = 9\Delta E^2/E_o^2$ (for $\alpha < 1/6$). The maximum current which can be forced through a tube with these focusing properties may then be expressed as $I_{max} = 38.5\ V_s^{3/2}\ 9\ \Delta E^2/E_o^2 \cong 350\ (\Delta E^2/E_o^{1/2})$. To obtain the monochromatized electron current, this expression must be multiplied by $\Delta E_{out}/\Delta E_{in}$.

References

1. C.E. Kuyatt and J.A. Simpson, Rev. Sci. Instr., 38(1), 103 (1967).

2. D. Langmuir in J.R. Pierce, Theory and Design of Electron Beams (D. Van Nostrand Company, Inc., New York, 1954).

3. I. Langmuir and K. Blodgett, Phys. Rev., 24, 49 (1924).